ORIGINAL PAPER

CrossMark

Spatial prediction of landslide-susceptible zones in El-Qaá area, Egypt, using an integrated approach based on GIS statistical analysis

Sara M. Abuzied[1] · Hamed A. Alrefaee[2]

Abstract
The spatial prediction of landslide susceptibility locations is a crucial task to support risk management and development plans in mountainous areas, such as El-Qaá area. The study aims to delineate landslide-susceptible zones that can cause enormous damage to property, infrastructure, and loss of life. An innovative integrated approach using remote sensing, geographic information systems, and geophysical techniques was used in the current work to evaluate landslide susceptibility locations. Magnetic data were supported by information derived from geologic, geomorphologic, topographic, and seismic data to reveal the landslides-prone zones. Several factors contributing to landslide susceptibility in El-Qaá area were determined, such as distance to faults, lithology, stream power index, slope, density of earthquake events, distance to epicenters, tilt derivative of magnetic data, distance to drainages, aspect, and topographic wetness index. A unique landslide susceptibility model (LSM) was developed in this study by integration all the spatial data that represent the contributing factors. The bivariate statistical index method was constructed to assign logic ranks and weights for the causative factors and their classes representing their realistic relations with landslide susceptibility in El-Qaá area. The landslide susceptibility map classifies El-Qaá area into five relative susceptibility zones: very high, high, moderate, low, and very low. The very high- and high-susceptibility zones are distributed in the eastern side of El-Qaá area where structurally controlled channels, steep topography to downhill lands, and Precambrian basement rocks are located. The resulting susceptibility map was tested and validated using the landslide locations that were delineated from field survey and satellite images at high resolution. The integrated methodology shows a more realistic landslide susceptibility map and adds a powerful tool to design a fruitful management plan in mountainous areas.

Keywords Remote sensing · Geographic information systems · Geophysical methods · Bivariate statistical analysis · Landslide susceptibility · Egypt

Introduction

Landslides are among the most destructive geo-environmental hazards in the mountainous regions such as El-Qaá area. Spatial prediction of landslide susceptibility locations becomes a necessary demand in arid regions because of population growth and the socio-economic impact of landslides (Abuzied et al. 2016a). Since the last century, the economic importance of

Sinai Peninsula has been augmented considerably (Fig. 1). El-Qaá area is one of the most hazardous areas in Sinai Peninsula given the susceptibility to a relatively high range of mass movements. El-Qaá area has captured the interest of many researchers as a strategic location for economic development (El-Nahry and Saleh 2004; Wahid et al. 2009; Sultan et al. 2013; Ahmed et al. 2014; Abuzied and Alrefaee 2017). Worldwide attention draws different studies for mapping landslide susceptibility due to urbanization growth in mountainous areas (Brabb 1984; Nilsen et al. 1979; Varnes 1984; Wagner et al. 1988; Aleotti and Chowdhury 1999; Guzzetti et al. 2012). Hence, the evaluation of landslide-susceptible zones in El-Qaá area is a highly important task for disaster management and planning development actions. The main aim of this study is the assessment of landslide susceptibility in El-Qaá area using a unique integrated approach based on remote sensing, geographic information systems (GIS), and geophysical methods.

✉ Sara M. Abuzied
saraabozied2@gmail.com; saraabozied@yahoo.com

1 Geology Department, Faculty of Science, Suez Canal University, Ismailia, Egypt

2 Geology Department, Faculty of Science, Kafr El-Sheikh University, Kafr El-Sheikh, Egypt

Fig. 1 Location map of El-Qaà area, southeastern Gulf of Suez, Egypt, using Landsat ETM+7
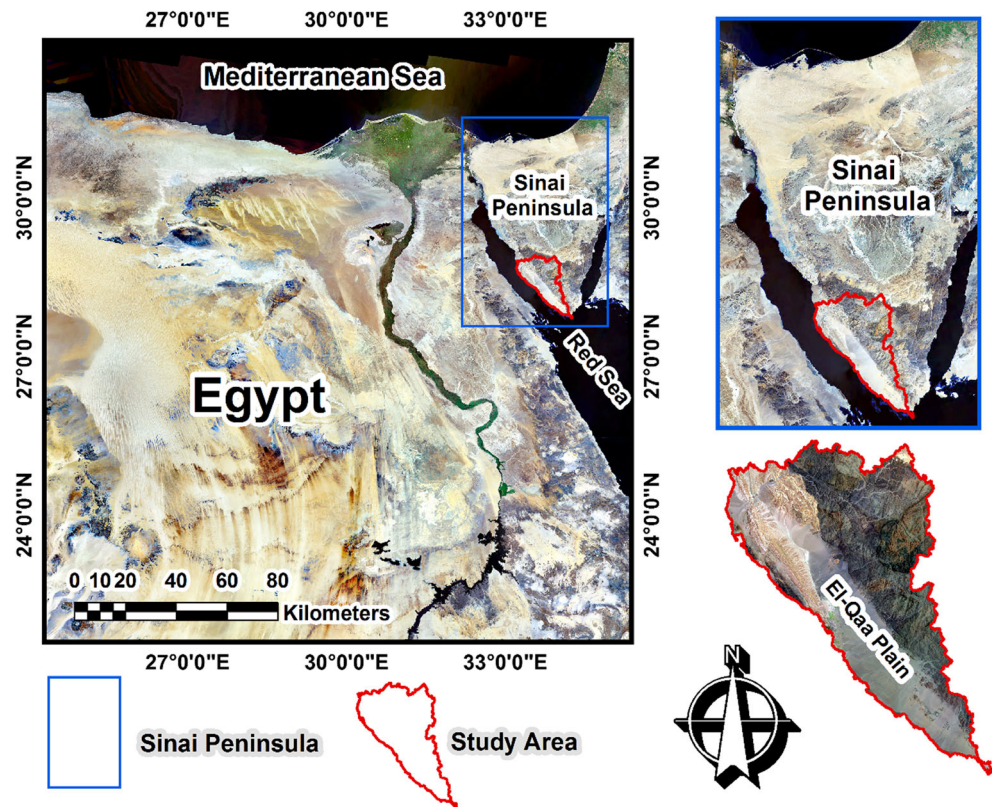
The integration of remote sensing and geographic information systems (GIS) has been widely applied to evaluate different geo-environmental hazards (Forte et al. 2006; Taramelli et al. 2010; Safaripour et al. 2012; Abuzied et al. 2016c). In addition, remote sensing and GIS technologies have been extensively used to assess landslide susceptibility (Wagner et al. 1988; Guzzetti et al. 2002; Sarkar and Kanungo 2004; Hong et al. 2007; Abuzied et al. 2016a). Several researchers around the world have supported geospatial mapping of landslide susceptibility using satellite image processing, geologic and topographic maps, and rectified ground truth data (Gorsevski et al. 2000; Baban and Sant 2005; Mancini et al. 2010; Gemitzi et al. 2011; Hadji et al. 2013). Geophysical techniques have been used in a few studies to evaluate zones prone to landslides (Bogoslovsky and Ogilvy 1977; De Vita et al. 2006). However, none of the studies conducted an integrated approach based on remotely sensed, geologic, geomorphologic, and magnetic data to evaluate landslide-susceptible zones and develop a model for spatial prediction. Geophysical methods help better understand geo-hazards and, hence, minimize their risks through accurate and proper planning. Geohazards are often unavoidable; hence, magnetic data interpretation reveals the subsurface geology to understand natural processes responsible for these threats and help to reduce their risks (Farooq et al. 2012; Bakhshipour et al. 2013). Incorporating geophysics into the analysis of natural hazards improves the characterization process and quantification of

the potential hazards (Kim et al. 2007; Bakhshipour et al. 2013; Fasani et al. 2013). Consequently, remediation strategies and plans adopt geophysical data interpretation to reduce and minimize the threats of natural disasters (Hunter et al. 2010; Malehmir et al. 2016). Although geophysical methods have been successfully employed in some examples for geo-hazards characterization, they are not commonly integrated into investigation schemes (Bogoslovsky and Ogilvy 1977).

The spatial prediction of landslide-prone zones in El-Qaá area is a challenging work because the topography is rugged and landslides are distributed in different locations in a vast area. Generally, landslides are caused by interaction of complex geological, geomorphological, and topographical factors (Chen and Wang 2007; Ilanloo 2012; Sankarapillai and Aslam 2013; Abuzied et al. 2016a). Using remote sensing techniques, it becomes possible to collect and analyze spatial and non-spatial data about factors influential in landslide susceptibility such as lithology, tectonic structures, slope, aspect, and distance to drainage (Carrara et al. 1991; Nagarajan et al. 1998; Saha et al. 2002; Abuzied et al. 2016b). Hence, the satellite image processing provides a suitable tool in this study to prepare maps ranked based on their contribution for mass movement occurrences (Varnes 1984; Guzzetti et al. 2012). Numerous remote sensing techniques were applied in the current study to extract the factors contributing to landslide susceptibility using various data sources such as the Shuttle Radar Topography Mission (SRTM), Landsat 7 [Enhanced Thematic

Mapper (ETM+)], and Landsat 8 [Operational Land Imager (OLI)] satellite images, geologic and topographic maps, and geophysical data. Abuzied (2016) supported the use of multi-spectral images such as Spot 5 and Landsat 7 to delineate lithological units, and land use/land cover in mountainous region close to El-Qaá area. SRTM data were used extensively in worldwide studies as a main source to extract several factors such as elevation, drainage network, stream power index (SPI), topographic wetness index (TWI), faults, slope, and aspect (Srivastava and Bhattacharya 2006; Kornejady et al. 2014; Pourghasemi et al. 2012; Abuzied et al. 2016d).

GIS is a powerful technology to manipulate and integrate the factors contributing to landslide susceptibility with great efficiency and accuracy (Saraf and Choudhury 1998; Bonham-Carter and Agterberg 1999). In the current study, several maps represent triggering and conditioning factors for the landslide susceptibility were constructed, analyzed, and integrated within the same georeferencing outline using GIS. The maps include fault buffers, lithology, SPI, slope, earthquake density, earthquake buffer, tilt derivative of magnetic data (TDR magnetic), drainages buffer, aspect, and TWI. Several GIS models including bivariate statistical analysis, logistic regression, fuzzy membership, and the analytical hierarchy process (AHP) were applied in different areas around the world for mapping landslide susceptibility (Saha et al. 2005; Wang et al. 2007; Gemitzi et al. 2011; Feizizadeh and Blaschke 2013). The simplest GIS model depends on a bivariate statistical analysis where the distribution analysis delineates landslide locations from satellite images and field survey, and thus provides information on the relation between landslide activities and their contributing factors. This model type represents the logical analytical method where the extracted landslide locations help to decide the numerical weights (Bughi et al. 1996). The bivariate statistical analysis represents a suitable method for mapping landslide susceptibility because the statistical method removes subjectivity in the qualitative analysis (Yin and Yan 1988; Saha et al. 2005). Hence, the GIS based on bivariate statistical analysis was applied in the current study to assign realistic ranks and weights for the landslide-contributing factors and their classes. The general goal of this study is to explore a unique landslide susceptibility model (LSM) integrating remote sensing, GIS, and geophysical techniques. The specific goals of this study are to correlate and match the landslide locations with the fault locations extracted from geophysical techniques. The correlation could verify the reality and accuracy of the model product.
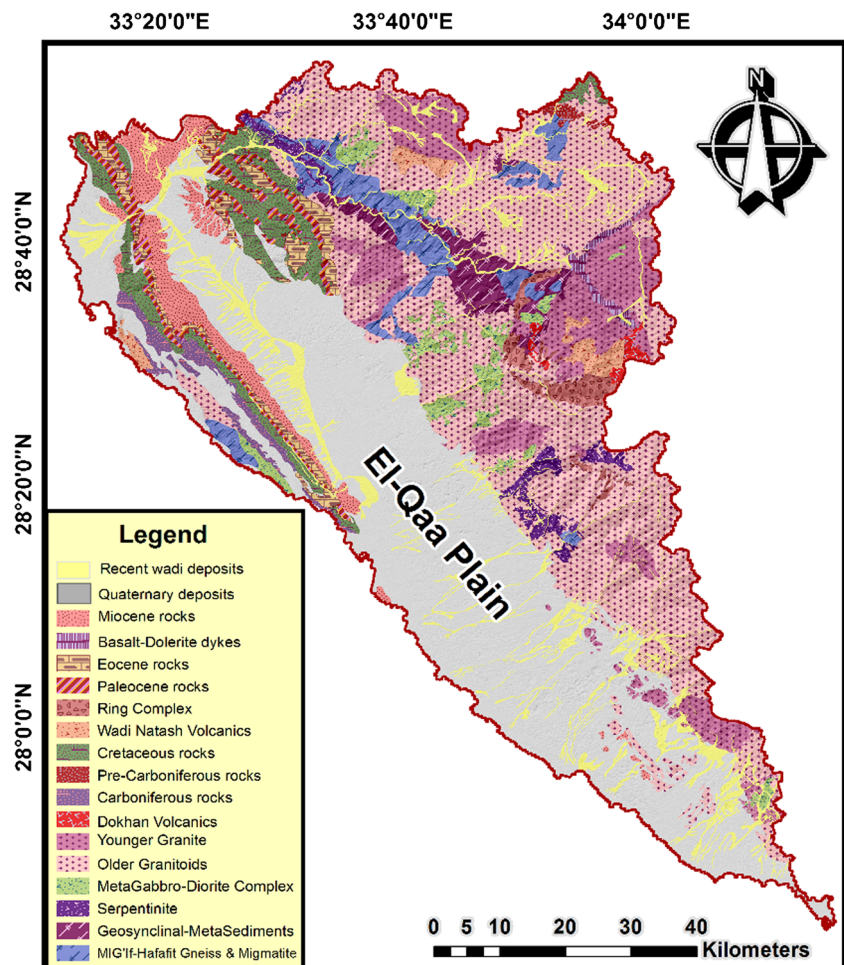
The study area

The study area is located between the southwestern side of Sinai rift zone and the southeastern Gulf of Suez coast (Fig. 1). El-Qaá area occupies 6070 km^2 and covers the area

between latitudes 27° 43′ 44″ to 28° 54′ 55″ N and longitudes 33° 11′50″ to 34° 15′ 24″ E. The study area represents 10% of the total area of Sinai Peninsula. El-Qaà Plain is an elongated coastal plain extending in the study and is 150 km long and 20 km wide (Fig. 1). The topography of El-Qaá area differs gradually from steep mountains to gentle plain, sloping towards the Gulf of Suez. Consequently, several hillslope processes including the movement of rock and soil by mass wasting occur in El-Qaá area. The relief varies in the study area from low zones to high rugged mountainous zones producing elevation from 100 to 2615 m. Several wadis representing separated drainage systems run over the study area. Various cycles of sedimentation created the wadis during Quaternary times and rainy periods (Gilboa 1980; Hammad 1980). Numerous active wadis drain through the study area such as W. Aat El-Gharby, W. Amlaq, W. El-Taalby, W. Timan, W. Asla, W. Feiran, and W. El-Aawag. The wadis play an important role in the erosional processes that occur in the southeastern coastal zone because the wadis are fed by seasonal floods (Wahid et al. 2009; Dames and Moore 1985; Sherief 2008).

El-Qaá area is characterized by an arid climate in which winters are cold with intense rain, and summers are dry and hot. 37 °C is recorded as the maximum temperature at El-Qaá area, while the lowest temperature may reach −3 °C in the highland regions such as Saint Catherine. The amount of precipitation increases in the eastern El-Qaá area where the average annual precipitation is recorded at about 80 mm. Sometimes, the precipitation occurs as snow on the high peaks. The flash floods occur seasonally in the study area due to convective rains (Dayan and Abramski 1983). The hydrographical basins in the eastern side of El-Qaá area are responsible for debris flow and mass movements because the eastern branches of their steep sloping channels drain from the highlands where high rates of rainfall prevail.

Geologically, El-Qaá area represents the western extension of the Precambrian Arabian-Nubian Massif that occupies the area extending from western Saudi Arabia to southern Sinai. The geological setting in the study area is classified to the northern granitic and sedimentary hills, and the South Sinai Mountains (Said 1962). The recent wadi deposits occupy 40% of the area creating alluvial fans, terraces, and wadi deposits. Several wadis are responsible for shaping the Quaternary alluvial fans when the stream velocity reduces quickly. The Precambrian basement covers approximately 46% of the area, and the Phanerozoic sedimentary succession covers the rest of the area (Fig. 2). The Precambrian basement rocks consist of igneous and metamorphic rocks which are highly weathered, and exist in hillslopes as fragmented blocks susceptible to movement when the shear strength is reduced. Commonly, the Precambrian basement rocks follow the steep hills along the main wadis, and the steep slopes accelerate rock fall accumulations into the wadis.

Fig. 2 Geologic map of El-Qaà area showing different lithological units (modified after Abuzied and Alrefaee 2017)

The structural setting of the study area is distinguished by two major tilted blocks called "Feiran Block" and "El-Qaá Block". The Feiran Block lies between two major faults and is situated between the eastern high mountains of the Sinai massif and the western lowland of El-Qaá Plain (Noweir and EL Shishtawy 1996). El-Qaá Block is covered by Quaternary deposits occupying the western side of El-Qaá Plain. Different types of faults affect El-Qaá area such as a few strike-slip faults, and mainly normal with subordinate oblique-slip components. Two major oblique-slip faults named G. El-Tur fault and Hadahid fault define the boundaries of the study area (Moustafa and Abdeen 1992). G. El-Tur fault is a Precambrian-Phanerozoic fault that exists on the eastern most side of El-Qaà Plain. The fault is the longest fault in the study area, extending more than 30 km, while Hadahid fault exists on the western side of the area extending to 20 km. In some places, Hadahid fault is hidden beneath the alluvium deposits of El-Qaá Plain. Other main fault trends are mapped in the area in addition to the two major faults. The faults trend in NW, NNW, NE, NNE, EW, and NS directions (Fig. 3a). The EW set is distinguished as the strike-slip fault (Noweir and EL Shishtawy 1996). The NW-SE and NE-SW faults represent

the dominant directions corresponding the common regional trends of the structures in El-Qaá area (Fig. 3a). The NW-SE faults cut the rocks into a series of sloping blocks susceptible to sliding. The blocks are commonly surrounded by synthetic normal faults dipping westward towards the Suez rift. In brief, the geomorphology, climate, and geology of El-Qaá area control the physical environment for landslide activities.

Materials and methods

A holistic approach was considered in the current study to delineate landslide susceptibility zones using geological, topographical, geomorphological, seismic, and geophysical data. These data were extracted from the following sources:

1. Geological maps (scale 1:250,000) were used to delineate different lithological units and define the training classes. The training classes were selected to support supervised image classification and accuracy assessment for the lithological map.
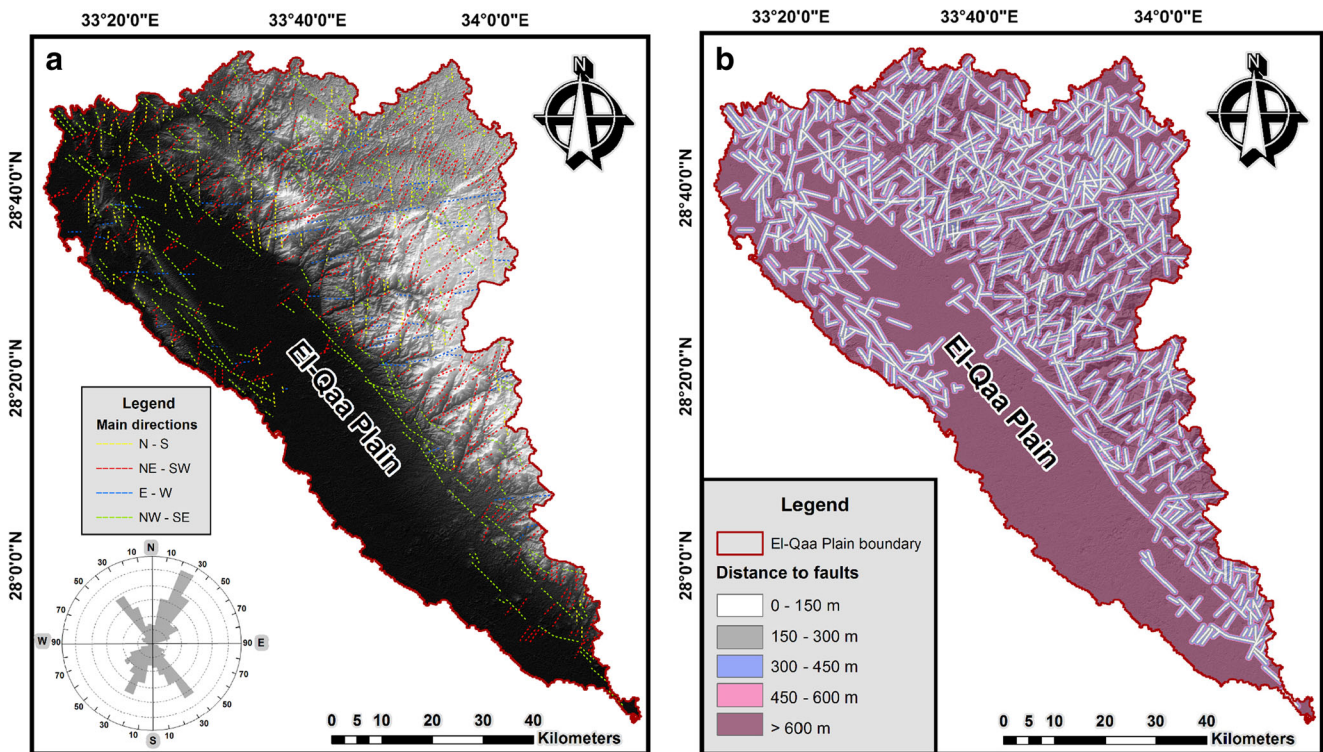
Fig. 3 **a** Fault map of El-Qaà area and rose diagram, revealing the different fault directions (modified after Abuzied and Alrefaee 2017). **b** Fault buffer map in El-Qaà area, southeastern Gulf of Suez, Egypt

2. Topographic maps (scale 1:50,000) were used to digitize main channels to guide the extraction of streams network.
3. SRTM data (spatial resolution of 29 m) was used to derive the topographic parameters such as elevation, slope, aspect, SPI, and TWI. The SRTM digital elevation model (DEM) supported the topographic maps in extracting the streams network.
4. ETM+7) Landsat satellite images acquired in May 2016 were selected to verify the extraction of streams network and major faults.
5. OLI Landsat 8 satellite images acquired in June 2016 was used to delineate various lithological units using several image processing methods.
6. Earthquakes data (1969–2016) acquired by the United States Geological Survey (USGS) were used to derive maps representing triggering factors such as earthquake buffers and earthquake density maps.
7. The aeromagnetic reduced-to-the-pole (RTP) map (scale 1:500000) acquired by the Geological Survey of Israel in (1980) was used to extract major faults and discontinuities.

Preparation of spatial database

Ten susceptibility factors contributing to landslide occurrences were suggested in this study as important data layers for the LSM. These layers were used to derive several maps including fault buffers, lithology, SPI, slope, earthquake density, earthquake buffers, TDR magnetic, drainage buffers, aspect, and TWI. The following paragraphs explain the preparation methods for these data layers.

Lithology

The lithological units in the study area were defined using remote sensing techniques and information from previous studies (Said 1962; Conoco 1982; Sherief 2008). The USGS website was used to download three scenes of OLI Landsat 8 satellite. The scenes were pre-processed to decrease the haze effects before mosaicking and sub-setting using ENVI 5.3 (Exelis, Boulder, CO, USA). Different image enhancement methods were performed with OLI 8 images to classify lithological units (Fig. 2). The processing methods include principal component analysis (PCA), independent components analysis (ICA), band ratio (BR) combinations, supervised classification, decorrelation stretch, and intensity hue saturation (IHS) transformation of red-green-blue (RGB) combinations (Abuzied and Alrefaee 2017). To obtain the highest contrast on lithological units, the combination of processing techniques was carried out to bands from each spectral zone such as visible, mid-infrared, and short-wave infrared (SWIR) II. Decorrelation stretch and IHS transformation were used to enhance bands 6, 7, and 4 (Abuzied and Alrefaee 2017). Moreover, PCA was used for all bands to evaluate the

principal component (PC) containing the most information. The best information was depicted from bands 6, 7, and 4. PC combination (3, 4, and 5) was produced to enhance lithological units and were compared to band ratio combinations. Algebra combinations and permutation were also considered to create band rationing. The contrast improved gradually using bands from various spectral zones such as bands 6, 7, and 4. The combinations 4/3, 6/2, and 7/3 supported the best contrast and were considered as the input for lithological classification (Abuzied and Alrefaee 2017). The processing techniques classify the study area to 18 rock units including Mig'if-Hafafit gneiss & migmatite, geo-synclinal metasediments, serpentine, metagabbro-diorite complex, older granitoids, Dokhan volcanics, younger granite, Carboniferous rocks, Pre-carboniferous rocks, Cretaceous rocks, Wadi Natash volcanics, ring complex, Paleocene rocks, Eocene rocks, basalt-dolerite dykes, Miocene rocks, Quaternary deposits, and Recent wadi deposits (Fig. 2). Most landslide locations are associated with the Precambrian basement rocks. The lithological map was reclassified into five classes based on the effect of each class on landslide susceptibility (Table 1).

Structural features

Faults, joints, and fractures represent a vital role for the mass movement scenario in the study area. Landslide occurrence can be commonly observed with proximity to tectonic structures. Fault locations act as the primary tracker for landslide-susceptible zones. Hence, the description of distances to faults is necessary to reflect hazard traces of higher landslide susceptibility. The purpose of structural analysis is to recognize the relationship between the locations of faults and zones highly susceptible to landslides. Different data sources including remotely sensed and geophysical data were used to extract the directions and depths of faults. Different software packages supported the extraction of faults such as ENVI 5.3, ArcMap 10.3, Oasis Montaj 7.0.1 (Geosoft Package 2008), and Rose Net.

The faults could be delineated from remotely sensed data such as ETM+7 and SRTM DEM, and from magnetic data. The extraction of major faults can be simply recognized within the image. Images from two sensors were utilized to trace the faults including three mosaic scenes of ETM+7 and four mosaic scenes of SRTM DEM. Firstly, an average low-pass filter (5 × 5) was carried out on all the bands of ETM+7 to remove any noise. Secondly, the Sobel gradient method was selected for edge detection because it has high efficiency to evaluate faults in different directions (Suzen and Toprak 1998). To reveal faults in their respective directions, a Sobel kernel with a pixel size of of 5 × 5 was applied along north (0°), northwest (45°), northeast (45°), and east-west (90°) directions. Furthermore, band ratios 5/1 and 6/2 were produced to enhance the texture property and clarify faults displacements in

combination with band 8. For slight enhancement, a non-directional Sobel edge detector was applied on band 8, and band ratios 5/1 and 6/2 (Abuzied and Alrefaee 2017). In addition, the mosaic scenes of SRTM DEM were used to create hillshade and to verify the extracted fault locations. The lengths and numbers of faults were analyzed in ArcMap 10.3; then, a rose diagram was used to define the relation between the orientations and lengths of faults (Fig. 3a).

Subsequently, a distance to faults map was generated using polygon mode under an ARC/INFO environment (Fig. 3b). The multi-buffer function was selected to define several buffer zones with a interval of 150 m representing the area of fault influence on the occurrence of landslides (Table 1). The fault buffer map was classified into five classes and converted to raster considering it as data layer (Fig. 3b). Based on the field studies, the classes were assigned suitable values representing the distances susceptible to landslides.

Topographic parameters

SRTM data were selected and processed to generate a DEM at a spatial resolution of 29 m. The DEM is considered as an essential data source to derive information on different topographic factors influencing landslide activity such as slope, aspect, SPI, TWI. Slope is one of the key factors with respect to landslide susceptibility. We generated the slope map using an SRTM DEM with a 29-m grid cell size and divided into 6 classes with equal intervals (Fig. 4a).

Aspect is a landslide-conditioning factor that has been considered in numerous studies (Ercanoglu and Gokceoglu 2004; Yalcin 2005). Some of the meteorological factors including amount of sunshine and rainfall directions could affect the slope stability, causing landside susceptibility (Mohammadi 2008). Generally, the hillsides receive dense rainfall, reaching saturation faster. Thus, the aspect factor is also suggested in this study to evaluate landslide-susceptible zones. The aspect map with a 29-m grid cell size was generated from the DEM (Fig. 4b). The aspect map was classified into nine categories namely, flat, N, NE, E, SE, S, SW, W, and NW. The aspect slope was reclassified to five classes according to the landslides distribution in each class (Table 1).

The SPI is also suggested as a landslide-conditioning factor because it is a measure of the erosive power of drainages (Conforti et al. 2011; Regmi et al. 2014). The SPI can be calculated using Eq. (1) according to the assumption that discharge (Q) is directly proportional to specific catchment area (A; Moore et al. 1991).

$$SPI = A \times \tan\beta \tag{1}$$

where A is the catchment area and β is the local slope gradient in degrees. The SPI map of the study area was produced using

Table 1 Spatial relationship between each landslide-contributing factor and landslide occurrences in order to calculate weights of a certain class i of factor k

Causative factors	Class	Npix (N_{ik})	Npix (S_{ik})	Densclas	Densmap	Densclas/Densmap	W_{ik}
Lithology	Wadi deposits & Miocene, Eocene & Paleocene rocks	1,833,041	860	0.0005	0.0064	0.0733	−2.613
	Pre-carboniferous rocks, Carboniferous Cretaceous rocks & basaltic-dolertic dykes	525,676	942	0.0018	0.0064	0.2801	−1.273
	Dokhan volcanics, Wadi Natash volcanic & ring complex	800,235	8363	0.0105	0.0064	1.6329	0.490
	Serpentinite, Mig'if Hafifite gneiss, meta-sediments & meta-gabbro-diorite complex	2,782,604	14,110	0.0051	0.0064	0.7923	−0.233
	Younger granite & old granitoids	1,273,528	21,902	0.0172	0.0064	2.6871	0.988
Distance to faults	< 150 m	1,978,916	37,368	0.0189	0.0064	2.9505	1.0820
	150–300 m	1,996,037	29,267	0.0147	0.0064	2.2910	0.8290
	300–450 m	1,860,983	22,322	0.0120	0.0064	1.8742	0.6282
	450–600 m	1,584,347	4514	0.0028	0.0064	0.4452	−0.8093
	> 600 m	7,679,688	3681	0.0005	0.0064	0.0749	−2.5917
Slope	0–12.3	4,760,022	12,407	0.0026	0.0064	0.4073	−0.8983
	12.3–24.68	1,426,016	17,867	0.0125	0.0064	1.9577	0.6718
	24.68–37.02	849,121	13,073	0.0154	0.0064	2.4056	0.8778
	37.02–49.36	174,665	2930	0.0168	0.0064	2.6211	0.9636
	49.36–61.7	5260	22	0.0042	0.0064	0.6535	−0.4254
Aspect	Flat (−1)	723,054	2571	0.0036	0.0064	0.5556	−0.5877
	E (67.5–112.5) & SE (112.5–157.5)	371,077	2194	0.0059	0.0064	0.9238	−0.0792
	S (157.5–202.5) & SW (202.5–247.5)	1,969,254	9643	0.0049	0.0064	0.7651	−0.2677
	W (247.5–292.5) & NW (292.5–337.5)	2,241,467	11,411	0.0051	0.0064	0.7954	−0.2289
	N (0–22.5, 337.5–360) & NE (22.5–67.5)	1,937,687	20,531	0.0106	0.0064	1.6556	0.5041
SPI	−12 to −7	1,759,955	2136	0.0012	0.0064	0.1896	−1.6627
	−7 to −2	1,047,700	9025	0.0086	0.0064	1.3460	0.2971
	−2 – 2	1,674,360	4510	0.0027	0.0064	0.4209	−0.8654
	2–7	2,366,322	23,443	0.0099	0.0064	1.5480	0.4369
	7–12	366,747	7185	0.0196	0.0064	3.0611	1.1188
TWI	< 5	1,776,193	16,281	0.0092	0.0064	1.4322	0.3592
	5–9	614,259	4652	0.0076	0.0064	1.1833	0.1683
	9–13	165,817	1225	0.0074	0.0064	1.1543	0.1435
	13–17	1,861,196	12,982	0.0070	0.0064	1.0899	0.0860
	17–21	2,797,619	11,159	0.0040	0.0064	0.6232	−0.4728
Distance to epicenters	600–1200 m	74	1	0.0135	0.0064	2.1115	0.7474
	1200–1800 m	224	5	0.0223	0.0064	3.4877	1.2492
	1800–2400 m	386	6	0.0155	0.0064	2.4288	0.8874
	2400–3000 m	507	5	0.0099	0.0064	1.5409	0.4324
	> 3000 m	30,372	185	0.0061	0.0064	0.9517	−0.0495

Table 1 (continued)

Causative factors	Class	Npix (N_ik)	Npix (S_ik)	Densclas	Densmap	Densclas/Densmap	W_{ik}
Density of earthquake events	1.80–18.15	266,192	2284	0.0086	0.0064	1.3407	0.2932
	18.15–34.51	69,119	929	0.0134	0.0064	2.1001	0.7420
	34.51–50.86	78,768	735	0.0093	0.0064	1.4580	0.3771
	50.86–67.22	80,623	410	0.0051	0.0064	0.7946	-0.2299
	67.22–83. 57	210,074	152	0.0007	0.0064	0.1131	-2.1799
TDR magnetic	1.5–0.9	98,047	455	0.0046	0.0064	0.7251	-0.3214
	0.9–0.3	25,459	113	0.0044	0.0064	0.6935	-0.3660
	0.3 to 0.3	29,013	284	0.0098	0.0064	1.5295	0.4249
	0.3 to –0.9	29,696	368	0.0124	0.0064	1.9363	0.6608
	–0.9 to –1.5	77,377	445	0.0058	0.0064	0.8986	-0.1069
Distance to drainage	< 100 m	571,644	7229	0.0126	0.0064	1.9759	0.6810
	100–200 m	520,274	3099	0.0060	0.0064	0.9307	-0.0718
	200–300 m	457,251	2061	0.0045	0.0064	0.7043	-0.3506
	300–400 m	391,027	1830	0.0047	0.0064	0.7312	-0.3130
	> 400 m	1,215,804	6065	0.0050	0.0064	0.7794	-0.2492

Map Algebra in ArcMap 10.3 and divided into five classes with equal intervals (Fig. 4c).

The TWI can also be recommended in this study as a landslide-conditioning factor because it refers to the effect of topography on the size and location of saturated zones generated by runoff (Pradhan and Lee 2010). The TWI can be calculated using Eq. (2) based on the relation between the slope gradient (in degrees) of the topographic heights (β) and the catchment area of each cell (A; Moore and Burch 1986).

$$TWI = \ln(A \times \tan\beta) \tag{2}$$

The TWI map of the study area was also created using Map Algebra in ArcMap 10.3 and divided into five classes with equal intervals (Fig. 4d).

Earthquake data

The earthquake events represent the triggering processes that cause landslide activities. Hence, the earthquake data from 1969 to 2016, including magnitude and depth, were downloaded from the USGS website. Distance to epicenters was considered as an important factor indicating landslide susceptibility. Therefore, the earthquake buffer map of El-Qaà area was prepared using ArcMap 10.3. The map was classified to five classes including 600, 1200, 1800, 2400, and 3000 m (Fig. 5a). The classes were selected based on the field observations and satellite image investigations to assign suitable distance for each class representing landslide susceptibility. The earthquake density map was also created using ArcMap 10.3 and classified to 5 classes from 1.8 to 83.5 (Fig. 5b). The kernel density analysis extension of ArcMap 10.3 was used to create the density map in order to evaluate the seismic anomaly activity in El-Qaà area.

Geophysical data

The RTP technique was used to create the total magnetic intensity map. The total magnetic intensity map was transformed to anomalies which could be measured if the field was vertical. The high-pass filter was performed in the RTP maps to increase the appearance of magnetic lows associated with the central basin of El-Qaà Plain. To delineate the fault trends, we performed the edge detection methods of the potential field data (Lahti and Karinen 2010). The TDR of magnetic data represents the ratio between the vertical derivatives (VD) of the magnetic. The TDR ratio was calculated using the formula (3) of Verduzco et al. (2004) to create the TDR data layer (Fig. 6). The TDR layer could be used as a crucial factor indicating faults, Precambrian basement rocks, and, thus, landslides occurrences.
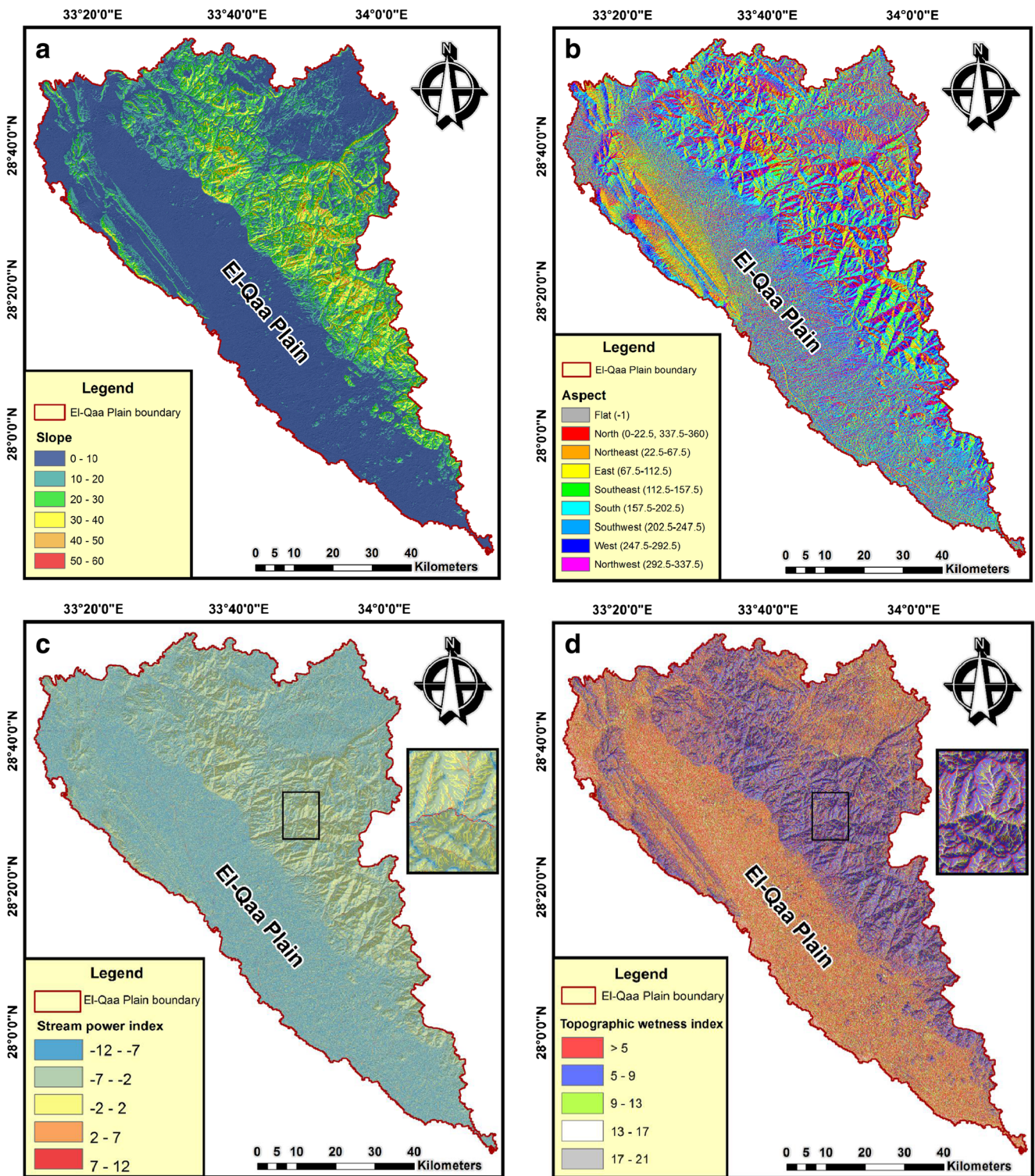
$$TDR = \tan^{-1}(VD/THDR) \tag{3}$$

Fig. 4 **a** Slope map of El-Qaà area, southeastern Gulf of Suez, Egypt. **b** Aspect map of El-Qaà area. **c** Stream power index map of El-Qaà area. **d** Topographic wetness index map of El-Qaà area

Drainage network

Topographic maps at the scale of 1:50,000 were rectified using ground control points (GCPs) and utilized to extract the main streams. The UTM coordinate system zone 36 was considered

for georeferencing all topographic sheets to integrate the data quickly in a GIS environment. The digitized streams were used as guide channels in terrain processing to extract drainages network. The ArcHydro tool of ArcMap 10.3 was used to generate watershed sub-basins and their streams. SRTM DEM
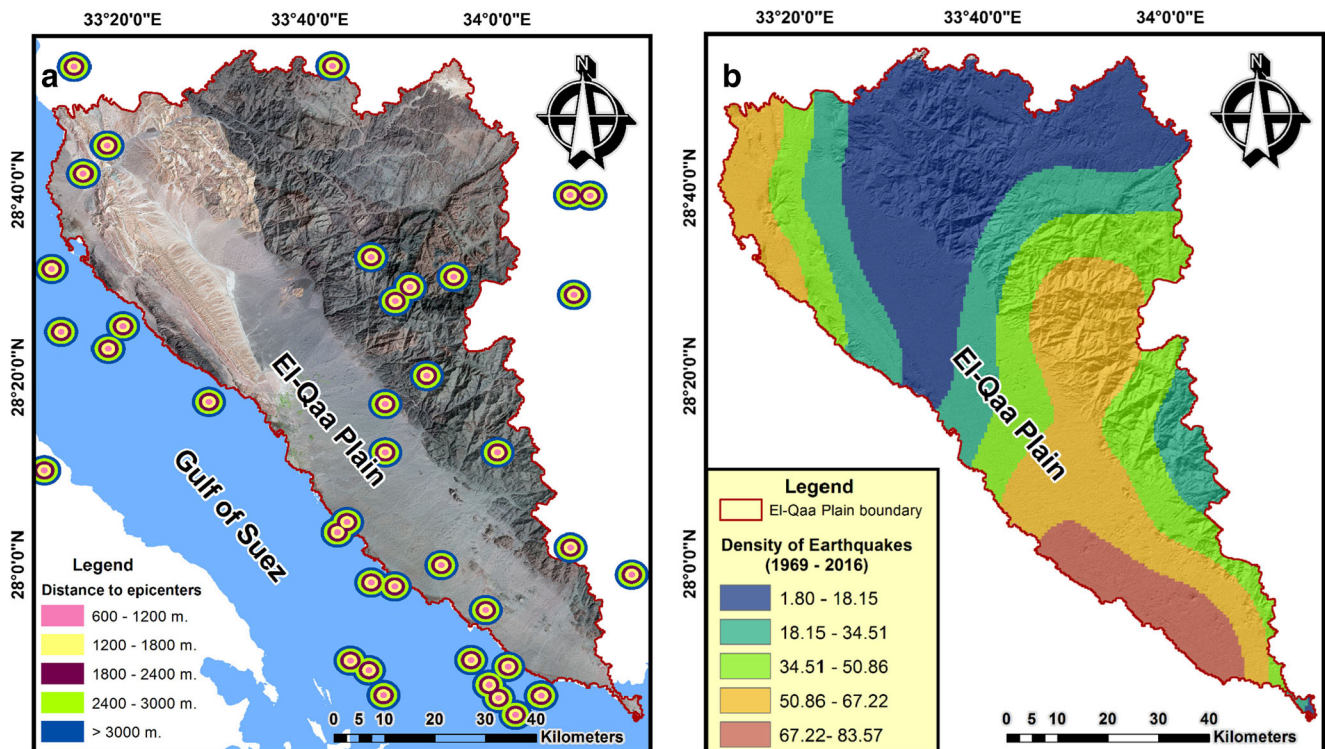
Fig. 5 **a** Earthquakes buffer map of El-Qaà area, southeastern Gulf of Suez, Egypt. **b** Earthquakes density map in El-Qaà area

was used as an input for terrain pre-processing to extract stream channels. ETM+7 was suggested in this study to verify the locations of digitized streams network. The drainages buffer map was prepared using polygon mode under an ARC/ INFO environment. The multi-buffer function was used to define several buffer zones with an of interval 100 m representing the area of stream influence on the landslide susceptibility. The drainages buffer map was divided into five classes and converted to raster considering it as data layer (Fig. 7). Based on field observations, the map was reclassified later into five classes reflecting the contribution of each class on landslide susceptibility (Table 1).
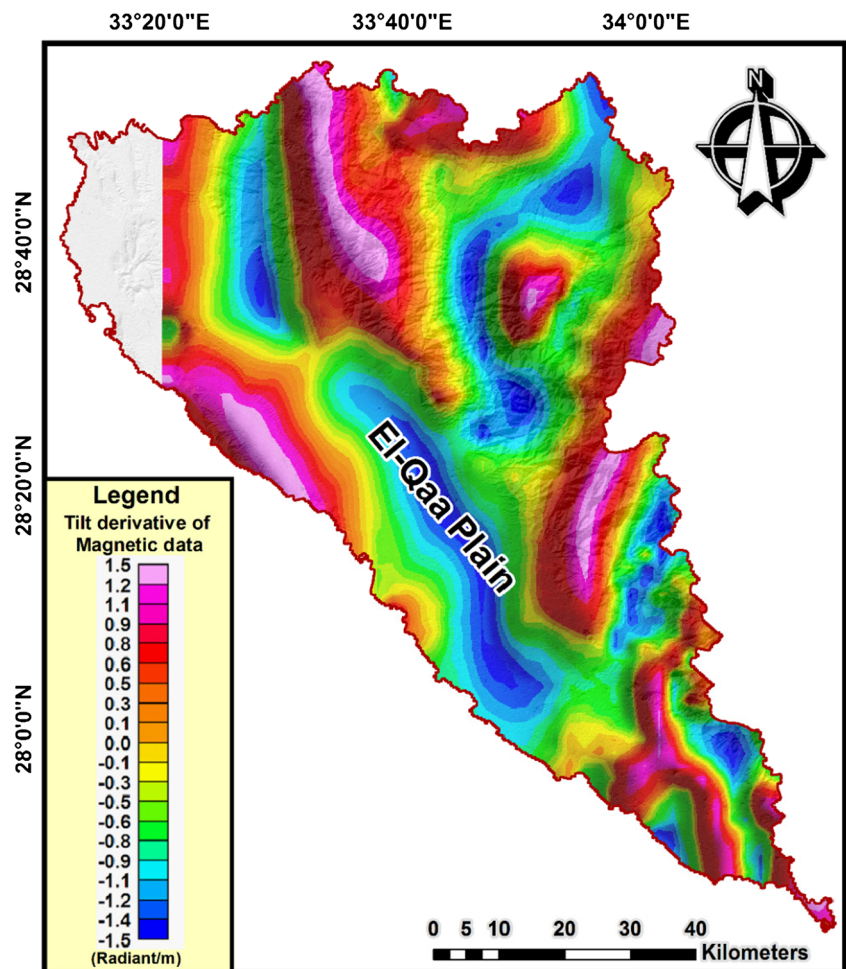
Landslide inventory

The landslide inventory map represents the backbone of the LSM in the current study. The inventory map is the primary source to provide information about the relationship between the landslides distribution and their causative factors (Fig. 8a). For example, some factors contributing to landslides in El-Qaà area were observed in the field such as the weathered rocks, structural features, and activities along drainage channels. The geospatial mapping of landslide susceptibility depends essentially on the accuracy and reliability of the collected data related to landslide locations. Since it is hard to reach all landslide locations in the mountainous area, the remote sensing images represent commonly suitable data source of information. Hence, the landslide inventory map could be

created using aerial photographs and satellite imagery analysis, and the field observations. The study area was divided into a grid shape to detect homogenously the distribution of all landslides. A total number of 680 landslide locations could be extracted from field observations and Google Earth images (Figs. 8a, b). Landslide locations extracted from these sources were digitized and later rasterized for further analyses using ArcMap 10.3 (Fig. 8a).

Obtaining a quality landslide inventory is an important task which depends on the inventory accuracy and on the information certainty in the map. Standards to define the inventory accuracy do not exist (Galli et al. 2008). The accuracy of a landslide inventory depends on the completeness and geographic precision of delineated landslides in the inventory map. The completeness is related to actual number of landslides in the study area compared to the landslides in the inventory map. The actual number of landslides in any area are typically unknown (Guzzetti et al. 2012). Completeness refers to the size of the smallest landslide reliably delineated in the inventory (Guzzetti et al. 2012). The landslide inventory map in this study displays small portrayed landslides (>20 m^2) and is thus nearly complete for landslides with small areas (Fig. 8). In addition, the field studies represent strong evidence to determine geographical precision (Malamud et al. 2004; Guzzetti et al. 2012). The geographical precision is related to the position and size of the landslides in the field compared to the geographical representation of the same landslides in an inventory map (Santangelo et al. 2010). Our landslide inventory

**Fig. 6** TDR magnetic map of El-Qaà area, southeastern Gulf of Suez, Egypt

map reveals the large portrayed landslides (>200 m^2) which were delineated from satellite images and field studies, and thus the inventory map is nearly complete for landslide locations in the study area (Fig. 8). The largest size of the landslide inventory corresponds to the size of the so-called Rollover which is actually the modal value within landslide size distributions (Guzzetti et al. 2002; Malamud et al. 2004).

Generally, landslide inventory maps are classified as geomorphological inventories, which are further classified to historical, temporal, and event inventories (Guzzetti et al. 2002; Malamud et al. 2004b). Landslides in El-Qaà area mostly take elliptical to circular shapes and exist in different types and scales (Figs. 8b, 13c). Due to the variation in the velocity and direction of material displacement, several types of landslides could be observed and recorded in El-Qaà area such as debris flow, rock fall, rock avalanches, and rock planar slides ("block slide" or translational landslides; Figs. 8b, 13c). According to the effect of triggering factors, these mass movements occurred progressively in a series of discrete landslide events where the blocks and debris moved over 160 m on hillslope, and rocks continued to fall from steep sloping terrains (Figs. 8b, 13c). Most of landslide occurrences have aerial

extents varying approximately from 100 up to 1000 m^2. The majority of landslides with large area occurred as debris flow on slopes varying from 24 to 37°. Some other landslide types including block slides and rock falls occurred on the hanging wall of the fault and on steep slopes varying from 37 to 45°. These types of landslides represent the most catastrophic events that threat the local inhabitants. The landslides distribution differs over the entire area, with maximum clustering in the eastern side of the El-Qaà area, while the western side shows limited landslide occurrences (Fig. 8a, b).

Debris flows represent significant hazards in mountainous terrain such as El-Qaà area. Debris flows are common landslides which occur traditionally in the same scenario in arid regions. The type of debris flows varies with movement of rock, boulders, and debris (Varnes 1978). These components have been mixed by geomorphic processes such as weathering (residual soil), mass wasting (colluvium), and explosive volcanism (granular pyroclastic deposits). Generally, debris flows are rapid to very rapid surging flows of saturated debris in steep drainage channels. Debris flows occasionally occur on existing paths, usually first- or second-order channels. Therefore, debris flow hazard exists in a particular path ending

Fig. 7 Drainages buffer map of El-Qaà area, southeastern Gulf of Suez, Egypt
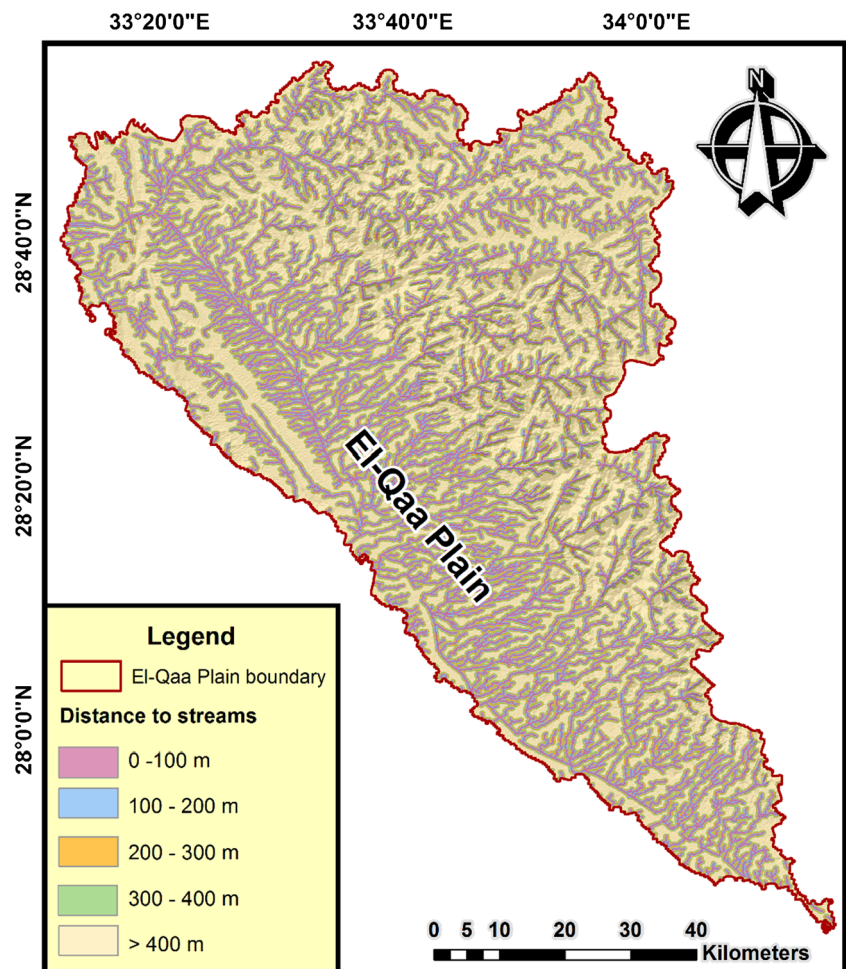

in a deposition area ("debris fan"). Different mechanisms initiate debris flow, such as the spontaneous instability of a steep stream bed (Cruden and Varnes 1996). Additional primary factors initiating debris flow include slides, debris avalanche, or rock falls from steep banks. In the landslide inventory map, 534 debris flows were delineated, representing 78% of the mapped landslide locations.

Rock fall generally represents the downward motion of rock fragment through the air. It occurs usually from very steep faces such as eroding stream banks in El-Qaà area. It may occur singly or in clusters, but there is little dynamic interaction between the moving fragments with the cliff path (Evans and Hungr 1993). Thus, this type of landslide represents individual fragments moving as independent rigid bodies (Cruden and Varnes 1996). Some large rock fragments in the study area separated from the depositing mass and rolled for 600 additional meters in the manner of a rock fall. Since the motion of these rock fragments are most hazardous, it is suitable to consider the entire event rock fall. By contrast, rock avalanches move in a flow-like manner as masses of fragments. Rock avalanche is essentially rapid and massive flow of rock fragments originated from a large rock slide or rock fall (Cruden and Varnes 1996).

Sometimes, the large rock slides break down rapidly during the downward motion along mountain slopes and thus travel as extremely rapid flows of rock fragments. The rock falls and rock avalanches occur at limited zones in the study area and are associated mainly with earthquake events. In the landslide inventory map, 81 rock fall events and 46 rock avalanches were delineated which represent, respectively, 11.8 and 6.7% of mapped landslide locations.

Rock planar slide ("block slide") is translational sliding of rock mass on a planar rupture surface (Cruden and Varnes 1996). The translational slides exist in the study area at different scales in sedimentary, igneous, and metamorphic rocks, but in limited distribution. This type of landslide usually occurs along fault planes and in igneous rocks with exfoliation (Cruden and Varnes 1996). The slide head separates rapidly from stable rock mass along a deep, vertical tension crack. Thus, the translational slides represent one of the most damaging landslides in El-Qaà area, especially when the block slides occur in igneous and metamorphic rocks. However, the block slides tend to be relatively slow in the case of sedimentary rocks and failures on very gently dipping discontinuity planes (12 to 17°). In the landslide inventory map, 39

Fig. 8 **a** Landslide inventory map of El-Qaà area, southeastern Gulf of Suez, Egypt. **b** The different types of landslide occurrences in El-Qaà area
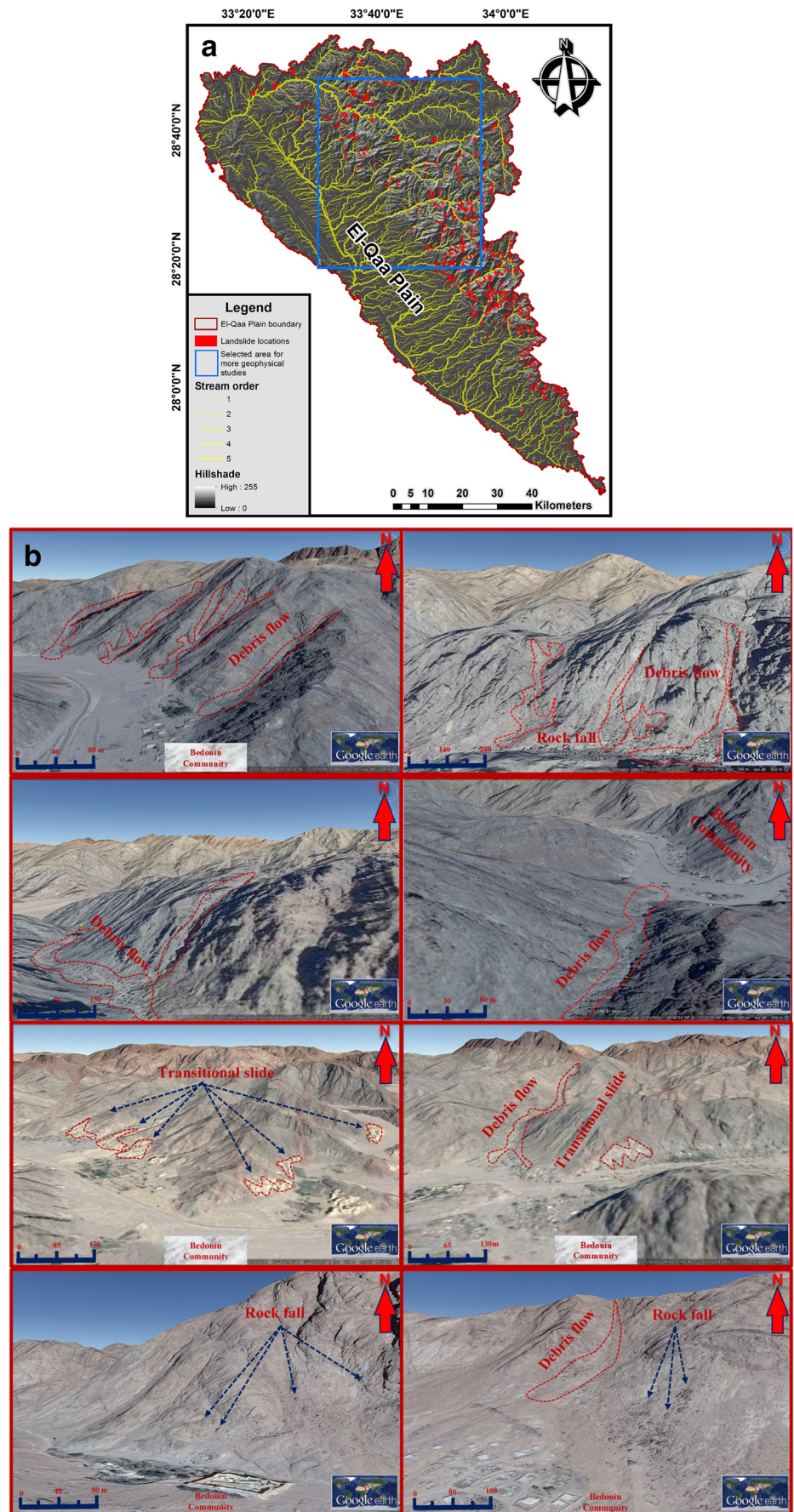
block slides were delineated which represent 5.7% of mapped landslide locations.

Based on the collected landslide locations, 73% of the collected data (500) were selected randomly to generate the landslide inventory map while the remaining 27% of the landslide locations (180) were used for testing and validating the model. It is obvious that most of landslide occurrences are associated with major fault trends in El-Qaá area. Hence, more geophysical investigations were applied in a small region of El-Qaà area (Fig. 8a) to evaluate the relation between the landslide zones and faults properties.

Modeling approach

For landslide susceptibility modeling, the previous geologic, topographic, seismic, and geophysical factors were integrated in accordance with their relative impacts to landslide activities. For that purpose, three main processes were recommended in the current study including ranking assignment to the causative factors, weighting assignment to the classes of each factor, and data integration to calculate the landslide susceptibility index (LSI).

Weighting process

The bivariate statistical index method depends essentially on a frequency analysis. It is the simplest statistical method to define the importance of each parameter class on landslide occurrence. This method provides information using the relation between the spatial distribution of parameter pixels and the landslide pixels. The index method could be easily obtained by dividing the landslide density for each class by the landslide density for the entire map (Eq. 4 and Table 1). The natural logarithm is carried out to assign positive weights when the landslide density is high and negative weights when the landslide density is low (Yin and Yan 1988). A weight value for each parameter class could be determined using the following equation (Van Westen et al. 1997):

$$W_{ik} = \ln \frac{Densclas}{Densmap}$$
$$= \ln \left[\frac{Npix(S_{ik})/Npix(N_{ik})}{\sum_{i=1}^{n_k} Npix(S_{ik})/\sum_{i=1}^{n_k} Npix(N_{ik})} \right] \quad (4)$$

where W_{ik} is the weight given to the ith class of a specific parameter (k), $Densclas$ is the landslide density within the parameter class, $Densmap$ is the landslide density within the entire map, $Npix\ (S_{ik})$ is number of class pixels containing landslides, $Npix\ (N_{ik})$ is the total number of pixels in a specific parameter class, and n_k is the number of classes in a parameter (K). The weights of all parameters classes were calculated according to the pixel values and tabulated in Table 1.

In the bivariate statistical index method, W_i can be calculated only for landslide occurrence classes because the method depends on the statistical correlation between the landslide inventory map and the causative parameters maps (Table 1). It means that no correlation will occur with the landslide inventory map in the absence of landslide pixels in a parameter class. The bivariate statistical index method was completely performed in the attribute tables of the causative parameters using ArcMap 10.3 software.

Ranking process

The index of entropy method was also performed based on the principle of bivariate statistical analysis to assign a rank for each input parameter (Vlcko et al. 1980). The parameter ranks were calculated from the defined level of entropy demonstrating the approximation to normal distribution of probability (Table 2). The parameter rank was considered as an entropy index representing the extent of influence of different parameters on the contribution of landslide susceptibility. We calculate the ranks R_k of the various contributing parameters using the equations by Constantin et al. (2011):

$$P_{ik} = A_b / A_a \quad (5)$$

$$Pr_{ik} = \frac{p_{ik}}{\sum_{i=1}^{n_k} p_{ik}} \quad (6)$$

$$H_k = -\sum_{i=1}^{n_k} Pr_{ik} \log_2 Pr_{ik}, k = 1, 2, \ldots, 11 \quad (7)$$

$$H_{kmax} = \log_2 n_k \quad (8)$$

$$I_k = \frac{H_{kmax} - H_k}{H_{kmax}}, I_k(1, 0), k = 1, 2, \ldots, 11 \quad (9)$$

$$P_k = \frac{1}{n_k} \sum_{i=1}^{n_k} P_{ik} \quad (10)$$

$$R_k = I_k \times P_k \quad (11)$$

Where P_{ik}, Pr_{ik}, and P_k are the probabilities of landslide density for class i of factor k, A_a is the percentage area of a particular parameter class, A_b is the percentage area of landslides in a particular parameter class, H_k and H_{kmax} are the entropy index values, I_k represents the information coefficient, and R_k is the resultant rank for the parameter as a whole.

Data integration

To determine the landslide susceptibility map, the rank value of each parameter was multiplied by the weights representing the numerical values of parameter classes as attribute information. The susceptibility map was created by summation of rank multiplications. The LSI for each 29 x 29-m cell was

Table 2 Ranking process for each causative factor in accordance with their relative impact on landslide occurrence

Causative factors	Class	A_a (%)	A_b (%)	P_{ik}	Pr_{ik}	H_k	H_{Kmax}	I_K	R_k
Lithology	Wadi deposits & Miocene, Eocene & Paleocene rocks	25.41	1.86	0.0733	0.0134	1.7313	2.3219	0.254	0.2781
	Pre-carboniferous rocks, Carboniferous Cretaceous rocks & basaltic-dolertic dykes	7.29	2.04	0.2801	0.0512				
	Dokhan volcanics, Wadi Natash volcanic & ring complex	11.09	18.11	1.6329	0.2988				
	Serpentinite, Migi Hafifite gneiss, meta-sediments & meta-gabbro-diorite complex	38.57	30.56	0.7923	0.1450				
	Younger granite & old granitoids	17.65	47.43	2.6871	0.4916				
Distance to faults	< 150 m	13.11	38.46	2.93	0.39	1.8532	2.3219	0.2019	0.3066
	150–300 m	13.22	30.13	2.28	0.30				
	300–450 m	12.32	22.98	1.86	0.25				
	450–600 m	10.49	4.65	0.44	0.06				
	>600 m	50.86	3.79	0.07	0.01				
Slope	0–12.3	65.97	26.80	0.4062	0.0506	2.0563	2.3219	0.114	0.1836
	12.3–24.68	19.76	38.59	1.9525	0.2433				
	24.68–37.02	11.77	28.24	2.3992	0.2990				
	37.02–49.36	2.42	6.33	2.6142	0.3258				
	49.36–61.7	0.07	0.05	0.6518	0.0812				
Aspect	Flat (−1)	9.98	5.55	0.5556	0.1183	2.2167	2.3219	0.045	0.0426
	E (67.5–112.5) & SE (112.5–157.5)	5.12	4.73	0.9239	0.1967				
	S (157.5–202.5) & SW (202.5–247.5)	27.19	20.80	0.7652	0.1629				
	W (247.5–292.5) & NW (292.5–337.5)	30.95	24.62	0.7955	0.1694				
	N (0–22.5, 337.5–360) & NE (22.5–67.5)	26.75	44.30	1.6556	0.3526				
SPI	−12 to −7	24.39	4.61	0.1891	0.0289	1.8752	2.3219	0.192	0.2520
	−7 to −2	14.52	19.49	1.3424	0.2050				
	−2–2	23.21	9.74	0.4198	0.0641				
	2–7	32.80	50.63	1.5439	0.2358				
	7–12	5.08	15.52	3.0530	0.4662				
TWI	<5	24.62	35.16	1.4284	0.2612	2.2764	2.3219	0.019	0.0214
	5–9	8.51	10.05	1.1802	0.2158				
	9–13	2.30	2.65	1.1513	0.2105				
	13–17	25.80	28.04	1.0870	0.1988				
	17–21	38.77	24.10	0.6216	0.1137				
Distance to epicenter	600–1200 m	0.23	0.50	2.1115	0.2007	2.2007	2.3219	0.0522	0.1098
	1200–1800 m	0.71	2.48	3.4878	0.3315				
	1800–2400 m	1.22	2.97	2.4288	0.2309				
	2400–3000 m	1.61	2.48	1.5410	0.1465				
	> 3000 m	96.23	91.58	0.9518	0.0905				
Density of earthquake events	1.80–18.15	37.77	50.64	1.3408	0.2309	2.0229	2.3219	0.1288	0.1496

Table 2 (continued)

Causative factors	Class	A_a (%)	A_b (%)	P_{ik}	Pr_{ik}	H_k	H_{Kmax}	I_K	R_k
	18.15–34.51	9.81	20.60	2.1003	0.3617	2.1959	2.3219	0.0543	0.0626
	34.51–50.86	11.18	16.30	1.4582	0.2511				
	50.86–67.22	11.44	9.09	0.7947	0.1368				
	67.22–83.57	29.81	3.37	0.1131	0.0195				
TDR magnetic	1.5–0.9	37.77	27.33	0.7235	0.1254				
	0.9–0.3	9.81	6.79	0.6920	0.1199				
	0.3 – -0.3	11.18	17.06	1.5262	0.2645				
	0.3 – -0.9	11.44	22.10	1.9321	0.3348				
	-0.9 – -1.5	29.81	26.73	0.8967	0.1554	2.1851	2.3219	0.0589	0.0601
Distance to drainage	<100 m	18.11	35.64	1.9676	0.3858				
	100–200 m	16.49	15.28	0.9268	0.1817				
	200–300 m	14.49	10.16	0.7013	0.1375				
	300–400 m	12.39	9.02	0.7282	0.1428				
	>400 m	38.52	29.90	0.7762	0.1522				

calculated using Eq. (12) where R_k denotes the rank for parameter k and W_{ik} denotes the weight of class i of parameter k.

$$\text{LSI} = \sum_{k=1}^{11} R_k \times W_{ik} \qquad (12)$$

## Geophysical data analysis

The magnetic data method is among the oldest geophysical techniques and has been principally employed for resources exploration. The magnetic method depends on density or magnetic susceptibility contrast to be successfully applied for mapping and characterizing the subsurface. The resolution power of the magnetic method is sensitive to near-surface anomalies and decreases with depth. Magnetic data has higher lateral resolution due to greater magnetic susceptibility contrasts than those of density (Malehmir et al. 2016). The magnetic method depends mainly on the prominence contrast of the magnetization and density in various geological circumstances (Sharma 1997). The RTP technique is applied to the total magnetic data to remove the distortion caused by variations in the azimuth and inclination of the magnetic field vector. The RTP technique converts the magnetic field to what it would be if the magnetization has a vertical direction. This transformation locates the magnetic anomalies correctly over the causative magnetic bodies' magnetization (Baranov and Naudy 1964).

The RTP map shows two NW-SE high magnetic trends at the western side (Fig. 9). The first occupies the northwestern corner (HM1) and the second occupies the southwestern corner (HM2). These two high magnetic trends confine a low magnetic anomaly (LM1) in between with an NW-SE axis at the southern part. The first trend (HM1) extends across the entire map, and its amplitude decreases close to its southern extension. The eastern half of the map shows an N-S broad regional low magnetic with an amplitude reaches to 499 nano-Tesla. The low magnetic trend is divided into four local anomalies (three lows; LM2, LM3, LM4, and one medium MM1). The eastern border of the map is occupied by an NE-SW high magnetic trend (HM3).

Separation of the residual anomalies

The top priority for exploration geophysicists is to separate the residual anomalies associated with local targets of geological interest such as mineral deposits, hydrocarbon accumulations, or shallow structural features. The residual anomalies are characterized by short wavelengths and small amplitudes due to small lateral extensions of their causative sources (Lowrie 2007). The magnetic map is obtained by applying a high-pass filter on the original RTP map to suppress the regional anomalies associated with deep, large sources (Griffin 1949).

Fig. 9 The reduced-to-pole total magnetic intensity map shows high magnetic (HM1, HM2, and HM3) and low magnetic anomalies (LM1, LM2, LM3, and LM4) with different amplitudes and directions
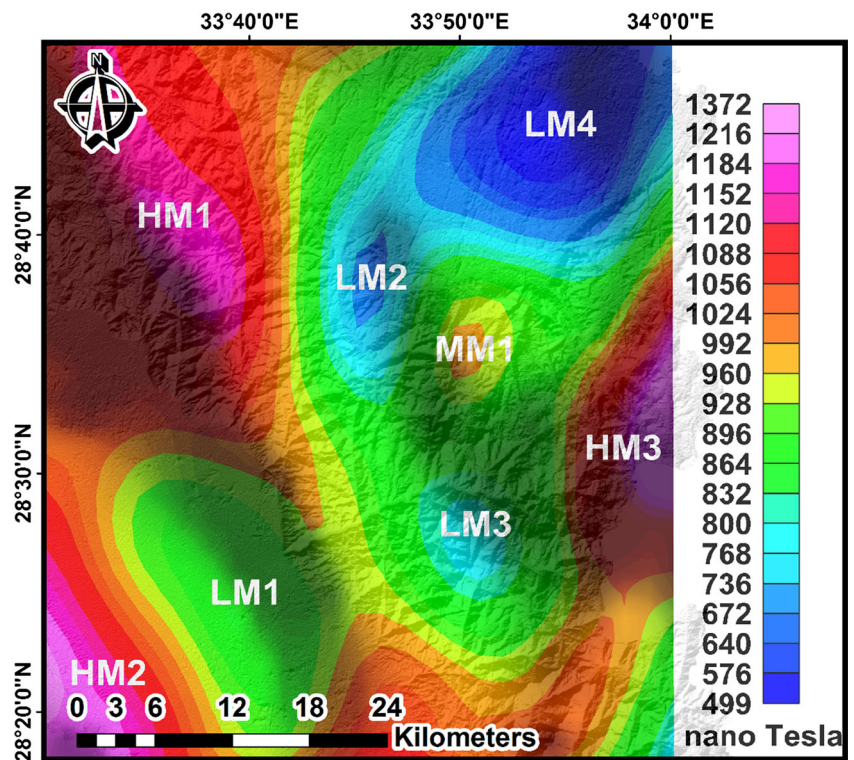
The RTP magnetic map with high-pass filter shows improvement of the residual magnetic anomalies compared to the original RTP map (Fig. 10). The positive magnetic trends (HM1) become clearer and extend further to the south. Also, (HM2, HM3, and MM1) became more visible. Moreover, a local high magnetic anomaly (HM5) occurred at the northern border. The NW-SE low magnetic trend (LMI) at the west is improved, extends farther to the northwest, and divides into two distinct local anomalies (LM1 and LM2). The three negative anomalies (LM2, LM3, and LM4) at the eastern side became distinguished.

Subsurface fault delineation

The magnetic method is important in mapping basement features such as faults, lineaments, lithological units, and intrusive units within the basement rocks buried beneath the sedimentary cover. These features localize and define zones of weakness and possible reactivation spots during new tectonic processes, and, therefore, they are vital to establishing critical human-made infrastructures. These structural features represent the primary targets of interest in engineering and environmental studies. Faults can be delineated either by sharp changes in the gradient of the anomaly signature or lateral disruption of anomaly patterns (Sharma 1997). In the current study, we use the edge detection methods and Euler deconvolution method to delineate the subsurface fault directions.

Edge detection methods The faults and boundaries of the subsurface causative magnetic sources are commonly delineated by the edge detection methods. The total horizontal derivative (THDR) shows magnetic maxima over the faults or boundaries of the causative sources while the TDR shows close to zero values over the faults or the boundaries and positive values over the centers of the sources (Miller and Singh 1994; Lahti and Karinen 2010). The TDR is the ratio between the vertical derivative (VD) of the magnetic to its total horizontal derivative (THDR) and can be calculated using Eq. (3) of Verduzco et al. (2004) as we discussed previously. The TDR of the magnetic data displays close-to-zero magnetic values that extend regionally in NW-SE direction at the western and central sides of El-Qaá area (Fig. 11). There is also an NE-SW pattern at the eastern side of El-Qaá area. Moreover, two line segments with an E-W pattern exists at the northern side, and three line segments with an N-S exist at the central side of El-Qaá area.

Euler deconvolution method Euler deconvolution is efficiently applied to define the location and depth to the magnetic causative sources (Thompson 1982). Euler's method outlines the magnetic boundaries, delineates fault trends, and defines the geometry of the magnetic causative source (Reid et al. 1990). The Euler deconvolution equation is formulated as:

$$(x-x0)\partial T/\partial x + (y-y0)\partial T/\partial y + (z-z0)\partial T/\partial z = N(B-T) \quad (13)$$

Fig. 10 The residual magnetic map created by using high-pass filter to the reduced-to-pole total magnetic intensity map. The high-pass filter shows improvements in the positive magnetic anomalies (HM1 to HM5) and the negative ones (LM1 to LM4)
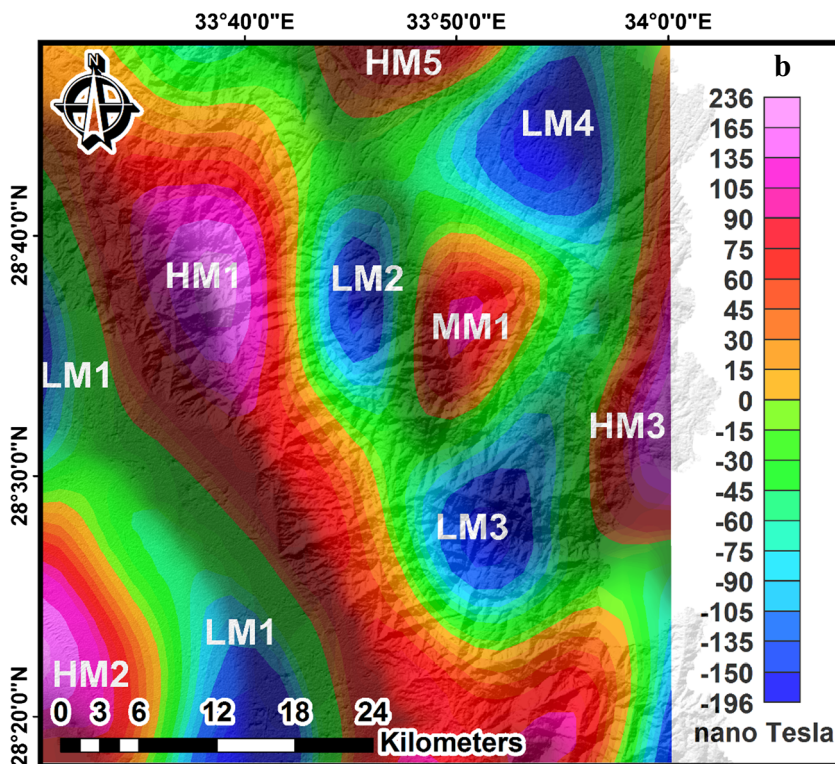
where T is the magnetic field measured at the position (x, y, z) and the causative magnetic source is located at the (xo, yo, zo). B is the regional field and N is the structural index (Thompson 1982). Euler deconvolution was applied to magnetic data using a structural index of zero (S.I. = 0.0) to emphasize faults as contacts (Fig. 12). Euler magnetic solutions are mainly clustered along NW-SE directions at the western part with another minor cluster at the eastern

Fig. 11 The tilt derivative of the magnetic data (TDR) shows close to zero magnetic values that extend linearly in the directions shown (white lines)
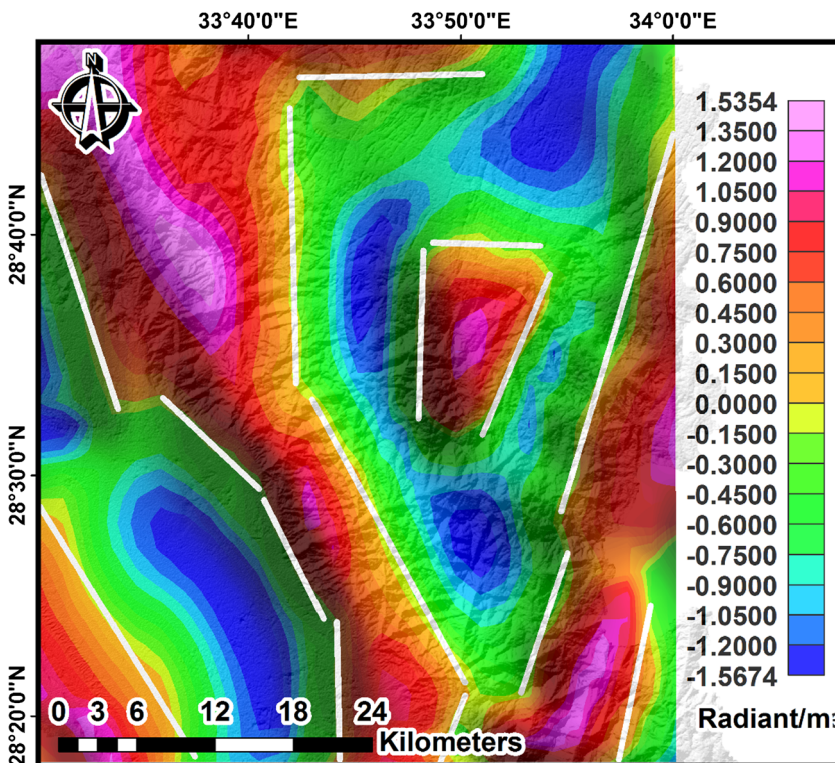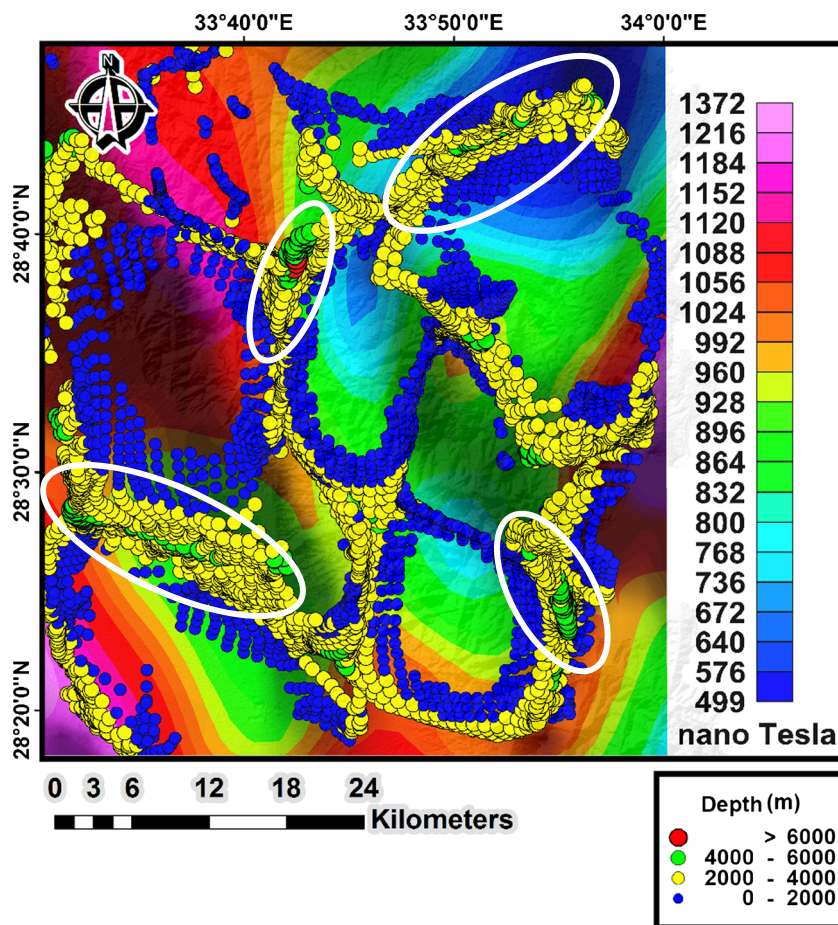
Fig. 12 Euler deconvolution of the magnetic data shows clustering of the magnetic solutions along NE-SW and NE-SW directions

part (Fig. 12). There are also many clusters along N-S directions, particularly in the southeastern and central sides. Also, there are clusters along the E-W direction at the northeastern, central, and southeastern sides. Finally, there is a cluster aligned in an NE-SW direction at the eastern boundary of the map. Besides delineating the fault directions, Euler deconvolution efficiently determined the depths to the basement. The depths to most of the magnetic solutions range from 0 to 4000 m with minor solutions between 4000 and 6000 m.

Results

The geospatial mapping of landslide susceptibility zones in El-Qaá area was achieved by combining the previously interpreted parameters through ranking and weighting processes. Based on the calculated weights and ranks, the influence levels of causative parameters were constructed. The structural factor representing the distance to faults, and lithological units, have the most influence on landslide occurrences (Tables 1 and 2). The SPI and slope values represent the following influential factors that cause landslide events (Tables 1 and 2). Usually, a magnetic survey is

needed to extract information about the basement relief, deep-seated structures, and the density of the sedimentary cap, which covers the basement within a constrain environment. In the current study, the magnetic reflect zones have deep-seated faults and Precambrian basement rocks which are more susceptible to landslides. Hence, magnetic data were supported by information derived from geologic, geomorphologic, topographic, and seismic data to reveal the landslide susceptibility locations.

The landslide susceptibility map classifies El-Qaá area into relatively different susceptibility zones. The resulting susceptibility map consists of five main classes varying from very low to very high susceptibility (Fig. 13a). The interpreted susceptibility map refers to the most susceptible zones to landslide occurrences. The most susceptible zones are mainly distributed in the eastern side of the mapped area where structurally controlled channels, steep topography to downhill lands, and Precambrian basement rocks exist. The very high- and high-susceptibility zones are located along several wadis and their tributaries in the study area such as Wadi Feiran, Wadi El-Aawag, Wadi Maier, Wadi Timan, Wadi Asla, and Wadi El-Mahasha (Fig. 13a). Most of these wadis are characterized by rugged topography and widely spread fault actions controlling the drainage distribution.
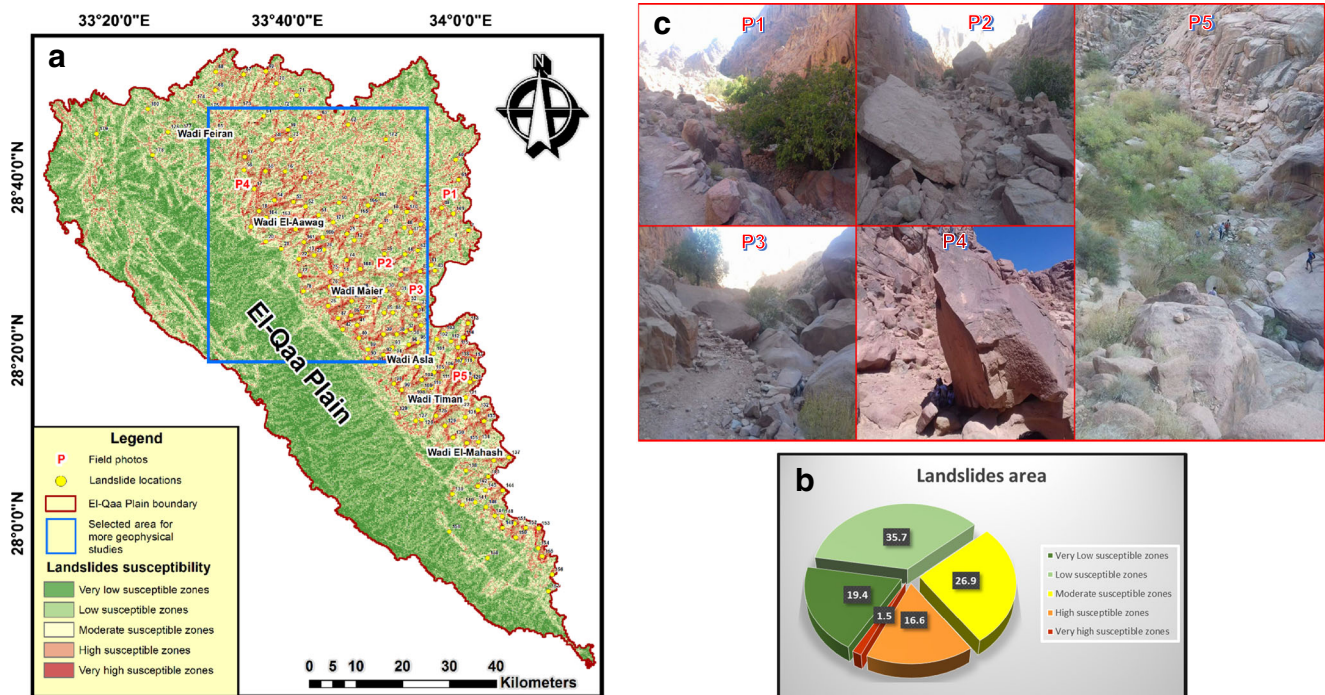
Fig. 13 **a** Landslide susceptibility map of El-Qaà area, southeastern Gulf of Suez, Egypt. **b** The percentage area of landslide-susceptible zones in the study area. **C** The distribution of landslide occurrences in El-Qaà area. The distribution mainly locates in very high- and high-susceptibility zones

The landslide susceptibility map was tested with the landslide locations that were delineated from satellite images and observed in the field survey to validate the final susceptibility map (Figs. 13a, c). Based on the correlation analysis, all landslide locations are associated with very high- and high-susceptibility zones. The landslide susceptibility map indicates that 1.5% of El-Qaá total area is very highly susceptible to landslides (Figs. 13a, b). The very high-susceptible zones occupy an area of 88.4 km^2 whereas the very low-susceptible zones occupy an area about 1175.2 km^2 (19.3% of the total mapped area). The moderate landslide-susceptible zones are distributed heterogeneously, covering 26.9% of the mapped area. The highly susceptible zones occupy 1007.9 km^2, representing 16.6% of El-Qaá area, while the low-susceptible zones occupy 2168.3 km^2, representing 35.7% of El-Qaá area (Figs. 13a, b).

The role of the faults on the landslides occurrence was clarified by more geophysical investigations on a small selected area (Fig. 13a). The geophysical investigations aim to explain the relation between the landslide-susceptible zones and fault distributions in El-Qaá area. The RTP map shows NW-SE high magnetic trends in the western part. Moreover, the RTP map shows an N-S regional low magnetic with several local anomalies at the eastern part. The analysis of the high-pass filter, TDR, and Euler deconvolution maps reveals that the area is dominated by NW-SE, N-S, E-W, and NE-SW faults. These faults exist at different depths varying from shallow faults up to 6000 m. Most of the deep faults (2000 to 6000 m) are associated with the NE-SW and NW-SE direction

(Figs. 12a, b). Most of the very high and highly susceptible zones follow these directions, reflecting the impact of fault depth on landslide occurrences (Fig. 13a). The highly landslide-susceptible zones exist in a few locations associated with N-S and E-W directions (Fig. 13a).

Discussion

Geospatial mapping of landslide susceptibility zones can be achieved through the investigation of various factors controlling landslide occurrences. The factors could be discerned from different data layers, including distance to faults, lithology, SPI slope, density of earthquake events, distance to epicenters, TDR magnetic, distance to drainage, aspect, and TWI. The influence of factors on the landslides varies spatially from one zone to another in the study area. The ranks and weights describe more precisely and quantitatively the variation in the influence of factors on the landslide occurrences (Tables 1 and 2). The integration of magnetic data adds the novelty and holistic nature of the approach to reveal the landslide-susceptible zones in mountainous regions.

Weight values

The weight values for the different classes of the causative factors display the importance of the respective classes in the landslide activities (Table 1). It can be observed from Table 1 that the lithological units have different weights representing

the contribution of each class in landslide activities. The Precambrian basement rocks, especially younger granite and old granitoids, have the highest weight (0.988), while the sedimentary succession, especially Miocene, Eocene, and Paleocene rocks, has the lowest weight (−2.613). Most of the Precambrian basement rocks have been exposed to an extended period of weathering, producing very vulnerable rocks for fracturing and sliding. The relationship between distance to faults and landslide occurrences reflects that the landslide probability is the greatest at the areas close to the fault. The maximum weight is 1.082 and can be observed at a distance <150 m. At a distance >600 m, the minimum weight is −2.5917, reflecting low landslide probability (Table 1). The structural features in the study area cause different degrees of stress, producing some weak zones in the weathered rocks. So, the areas close to the fault are the zones most susceptible to landslides.

In case of slope angles, the highest weights are 0.8778 and 0.9636 observed in slope ranging from 24.6° to 49.3°. The terrain sloping from 37 to 49 has been exposed to several types of landslides in which rock falls exist in the highest degree (>45), and several slides and debris flows also exist in degrees less than 45 (45 refers to the beginning of the transport zone). Furthermore, the terrain sloping from 24 to 37 is characterized by a few slides and several debris flows. Slides generally occur in moderately inclined slopes and along a well-defined shear plane. The lowest weight can be observed in very gentle slope class (0° – 12.3°) and very steep slope class (49.36° – 61.7°) assigning −0.8983 and − 0.42,54 respectively (Table 1). Generally, the landslide activities increase with the increase of slope gradient up to a particular extent, and then decrease (Sun 2009; Kanungo et al. 2011). Within the aspect classes, the highest weight is 0.5041 for north- and northeast-facing slopes followed by east- and southeast-facing slopes (−0.0792). Flat, and south and southwest have the lowest weight assignations of −0.5877 and −0.26,77 respectively (Table 1). Sometimes, the slope areas facing the afternoon sun have the highest temperature, affecting the amount of water evaporated or absorbed by the soil. Therefore, some slope areas facing the afternoon sun have less soil moisture, less vegetation cover, and thus much erosion may occur. Hence, north- and northeast-sloping areas have the highest weight in this study.

In the case of SPI, the maximum weight is 1.1188 for the highest value of SPI (7–12) indicating a high probability of landslide activities, while the minimum weight is −1.6627 in the lowest value for SPI (−12 to –7), indicating a low probability of landslide activities (Table 1). The erosive power of water flow depends on the assumption that discharge increases with the increase of catchment area and slope gradient (Moore et al. 1991). Therefore, the high values of SPI cause a high probability of landslide activities. It can be observed that the maximum weight of TWI is 0.3592 for the lowest value class

(<5). However, the minimum weight of TWI is −0.4728 for the highest value class (17–21). Commonly, sediment transportation increases with the increase of catchment area and slope gradient. Hence, the higher slope gradient relatively gives lower TWI and higher landslide probabilities. For the relationship between distances to drainage and landslide locations, the closer drainage, the greater the landslide probability. At a distance about <100 m, the maximum weight is 0.681, indicating a high probability of landslides, and at distances about >400 m, the weight is −0.249, indicating a low probability. The erosional and torrential activities are usually associated with drainage and, thus, areas close to drainage are highly exposed to landslide activities.

Earthquake events represent triggering processes that cause different types of landslides in the study area. There is no doubt that the closer the epicenter, the greater the landslide susceptibility. At a distance about <600 m, the maximum weight is 0.7474, indicating a high susceptibility of landslides, and at distances about >3000 m, the weight is −0.0495, indicating a low susceptibility. Commonly, a higher density of earthquakes events indicates higher landslide vulnerability. However, the maximum weight is 0.7420 at a density about 34 m/m^2 because the highest density of earthquakes is concentrated in the Gulf of Suez and in the sedimentary rocks at the western side of the study area.

For TDR magnetic factor, the maximum weight could be observed in the intermediate classes (0.3 to –0.9 and 0.3 to –0.3), assigning 0.661 and 0.425, respectively. While the minimum weights are calculated for the classes of the highest and lowest values (0.9–0.3, 1.5–0.9, and −0.9 to –1.5), assigning −0.366, −0.321, and −0.107, respectively. The magnetic data is commonly used to reveal the subsurface structures. Most of the classes having high weights can easily reflect the locations of major faults in the study area. Hence, the weight assigned for the different classes of TDR layer represents the logic value for its contribution in LSM.

Rank values

The rank values for the causative factors reflect the importance of the respective parameters in the landslide activities (Table 2). From Table 2, the distance to faults has the highest impact in the landslide susceptibility (0.3066) followed by lithological units (0.2781). The rank of structure features represents the realistic reflection of a fault's contribution to landslide activities. Generally, faults create weakness zones characterized by heavily fractured rocks, indicating landslide susceptibility. Hence, any water movement along fault planes promotes the erosional processes such as mass wasting and overland flow. Several landslide types could be observed at the distances close to faults. All the slides occur close to the fault and on the shear plane. Furthermore, most of El-Qaà channels are structurally controlled. Hence, most of debris

flows also occur along the fault plane. For lithology, the different lithological units have dissimilar resistant properties, reflecting various landslide susceptibility values. For example, the Precambrian basement rocks are highly weathered and heavily fractured. Usually, the rock disintegration induced by weathering on sloping terrain reduces the shear strength in the slope interior supporting the landslide activities. In addition, the weathered and disintegrated rocks in the vicinity of structural features boost water flow along steep sloping channels during rains. Several landslide types are associated with Precambrian basement rocks. In the steep sloping terrain, rock falls exist mainly with younger granite and old granitoids. In the terrain sloping from 24 to 37, slides and several debris flows exist, mainly with different lithological units of Precambrian basement rocks. Therefore, most of the landslide-prone zones are distributed in this rock type.

The SPI has also a high impact in the landslide susceptibility (0.2520) followed by slope gradient (0.1836; Table 2). As we discussed previously, the SPI depends essentially on the slope gradient and the catchment area. Thus, the amount and the velocity of water draining from upslope areas increase with the increase the catchment area and the slope gradient (Moore et al. 1991). Therefore, the potential erosive power of overland flow can be commonly defined by SPI (Moore et al. 1993). The variation of slope angles represents a key factor to analyze slope stability and, thus, indicating landslide occurrences (Lee and Min 2001). Hence, the slope map was created to reveal slope classes in which the landslide occurred. The result reveals that about 39% of the landslides, especially debris flows, occurred on slopes ranging from 12.3 to 24.6° (Table 2). However, 61% of the landslides occurred on slopes ranging from 24.6 to 49.3°. These landslides include debris flows, slides, and a few rock falls.

Seismic activity is the critical triggering factor causing landslides in the study area. Most of landslide locations are associated with old earthquakes events. The rank of earthquakes density is 0.1496, reflecting the contributions of old earthquake events in landslide occurrence. Furthermore, the rank of distance to epicenter is 0.1098, indicating closer proximity to an epicenter results in higher landslide vulnerability. Commonly, zones close to epicenters are highly fractured and jointed, indicating greater probability of landslides in the mountainous regions.

The ranks of TDR magnetic data and distance to drainages are 0.0626 and 0.0601, respectively (Table 2). TDR magnetic data usually reflects the locations of subsurface faults that play a vital role in triggering landslides because tectonic breaks usually decrease the rock strength, increasing the probability of landslides. The drainage features represent a greater potential for surface flow and soil erosion, resulting in more landslides. The drainage may affect the slope stability by eroding the downhill slopes, and may contribute to landslide activities by saturating the lower part of material until a critical water

level is reached. Therefore, distance to drainage is also considered in the predictive model.

The ranks of aspect and TWI were assigned the lowest values of 0.0426, and 0.0214, respectively (Table 2). Aspect is a landslide conditioning parameter that indirectly affects slope stability, and plays an integrated role with some meteorological events, including the direction of rainfall and amount of sunshine, which result in slope failure. In some cases, hillsides reach saturation faster because these sides receive dense rainfall. However, this status depends on infiltration capacity which is controlled by different factors including topographic slope, soil types, permeability, porosity, and amount of sunshine. Consequently, slope-forming material facilitates water infiltration, producing a buildup of hydrostatic pressure. Hence, the aspect may have different indications that reflect landslide occurrences in the study area, and thus it deserves the given rank. TWI is considered as a topographic factor within the runoff model. TWI refers to the topographical impact on the location of saturated areas by runoff.

Geophysical perception

The sources of geo-hazards are sometimes invisible; hence, magnetic data interpretation reveals the subsurface geology and enables understanding of natural processes posing threats (Bakhshipour et al. 2013). Furthermore, maps of magnetic anomalies reveal structures and trends that may control geological hazards such as landslides (Benson and Floyd 2000; Oehler et al. 2004). Study of geologic hazards often relies on the use of magnetic data interpretation to detect faults and evaluate their size (Bogoslovsky and Ogilvy 1977; Malehmir et al. 2016). The NW-SE magnetic lows at the western part can be related to thick sediments of the El-Qaá Plain basin. This conclusion is supported by several geophysical studies by Sultan et al. (2013), Ahmed et al. (2014), Azab and EL-Khadargy (2013), and Abuzied and Alrefaee (2017) who investigated sedimentary cover with a thickness ranging from 2.5 to 3.5 km. The sedimentary rocks have lower densities and magnetic susceptibilities than those of Precambrian basement rocks (Dobrin 1976; Dobrin and Savit 1988).

The magnetic map reflects several local anomalies with different polarities and sizes. These local anomalies can be interpreted by the existence of small, shallow structural and geological features with distinct densities and magnetic susceptibilities (Griffin 1949; Dobrin 1976; Lowrie 2007). These structural and geological features exist within the sedimentary cover as anticlinal and synclinal structures or within the basement rocks as intrusion bodies (dikes and sills) near the ground surface. The maps also reflect the alignment of magnetic anomalies in NW-SE, N-S, E-W, and NE-SW directions. The linear magnetic pattern with close-to-zero values defined by the TDR map reflect possible faults that trend in NW-SE, NE-SW, E-W, and N-S directions. Furthermore, the magnetic

solutions are clustered along faults that trend in the same previous trends delineated by the TDR map. These faults define the boundaries of structural and geological features that were developed by tectonic events that dominated the area during its geological history. The Sinai Peninsula as a part of North Egypt was subjected to numerous tectonic events. The East African tectonic events represented the oldest tectonic movement that occurred in the Precambrian time and was responsible for N-S structural features and faults (Dennis 1984; Abu El-Ata 1988; Meshref 1990). The opening of the Neotethys (Mediterranean Sea) in the Middle Jurassic due to the separation of the European plate from the African plate resulted in E-W faults (Abu El-Ata 1988; Sultan and Halim 1988; Meshref 1990). Also, the opening of the Red Sea and Gulf of Suez during the Late Oligocene-Early Miocene time resulted in the NW-SE fault system (Colletta et al. 1988; Patton et al. 1994). By the Late Miocene time, the Gulf of Aqaba was formed due to NE-SW strike-slip movement along the Dead Sea-Aqaba transform fault system (Mosconi et al. 1996). It is clear that most of the landslide occurrences associated mainly with the NE-SW and NW-SE faults (Fig. 13a). The depths of these faults reach up to 6000 m in some locations (Figs. 12), reflecting their role in landslide susceptibility (Fig. 13a). The landslide occurrences can be observed in a few locations associated with the N-S and E-W faults (Fig. 13a). Hence, the tectonic movements that cause the opening of Gulf of Aqaba and Gulf of Suez represent one of the main reasons triggering landslides in El-Qaá area.

Landslide susceptibility map and its validation

The visualization of landslide-susceptible zones could be achieved through the integration of all the previous factors considering ranks and weights of the causative factors and their classes. The landslide susceptibility map was classified into susceptibility classes using the natural breaks method in ArcMap 10.3. The map was categorized into five classes: very low-, low-, moderate-, high-, and very high-susceptibility zones (Fig. 13a). The landslide susceptibility map defines zones very highly susceptible to landslides, which occupy 1.5% of the El-Qaá total area (Figs. 13a, b). The very high-susceptible zones are distributed in the eastern side of the study area where structurally controlled channels, steep topography to downhill lands, and Precambrian basement rocks exist. The highly susceptible zones cover 16.6% of El-Qaá area and are mainly distributed in the Precambrian basement rocks, which are highly weathered and heavily fractured (Figs. 13a, b). The moderately susceptible zones are in different areas, covering 26.9% of the El-Qaá area (Figs. 13a, b), and located in lands with a slope ranging from 0 to 12.3° and in some lands with a slope ranging from 49.36 to 61.7°. The very low- and low-susceptible zones occupy 19.3 and 35.7%, respectively (Figs. 13a, b). These zones are distributed abundantly on the western side of the study area and around the El-Qaá Plain. These zones are mainly covered by fresh sedimentary rocks with minor fractures.

The susceptibility map was tested using existing landslide locations data for the study area which were derived from field survey and satellite images (Fig. 13c). A total of 180 landslide sites in El-Qaá area were plotted in the landslide susceptibility map to validate the output of this study (Fig. 13a). A good correlation could be noticed between the recent landslide locations and zones defined as highly susceptible. The very high- and high-susceptibility zones cover all the landslide occurrences that mainly occurred close to faults and active drainages, and in the unstable slopes composing of Precambrian basement rocks (Figs. 13a, c). The faults are a dominant factor in landslide activities where they strongly affect the landscape dynamics and geology of El-Qaá area initiating slope instabilities. The geophysical studies also confirm these facts and reveal the depths and directions of major faults that may cause the landslide events.

Briefly, the scenario of different types of landslides in El-Qaà area can be interpreted as gradual occurrences. There are two failure mechanisms in the study area, including shallow and deep sliding failures. The deep sliding failure develops firstly when bedrock fails along a discrete plane of weakness, like a fault, due to a triggering factor such as an earthquake. Deep sliding failure occurs as a rock fall or block slide at steep slopes and represents the most catastrophic type. In some cases, the large block slide or rock fall may gradually create a massive flow of rock fragments, resulting in a rock avalanche. All these types exist in a relatively few locations in the study area close to earthquake epicenters. However, the shallow sliding failure develops when surficial soil and saprolite crack on a steep hillside produce slow pre-failure deformation. Then, the sliding mass accelerates, disintegrates, and widens through entrainment, forming a flow-like debris avalanche. The avalanche enters a drainage channel pervading more saturated soil and is thus converted to a surging debris flow. The debris flows distribute in many locations in El-Qaà area and represent the most common landslide occurrence that threatens the local inhabitants and cultivation lands.

Conclusion

The development of a predictive model for landslide susceptibility in El-Qaá area is the main outcome of the current study. The LSM was built based on 10 causative factors indicating landslide occurrences. The factors include distance to faults, lithology, SPI, slope, density of earthquake events, distance to epicenters, TDR magnetic data, distance to drainages, aspect, and TWI. The ranks and the weights for the contributing factors and their classes were assigned based on bivariate statistical analysis. Several landslide locations were extracted from

field observations and Google Earth images to create the landslide inventory map. Most of landslide occurrences were recorded in association with the faults locations. Therefore, we consider the magnetic data in this study to provide more details. The selected factors were spatially integrated to calculate the LSI for each 29 x 29-m cell.

The landslide susceptibility map was created in which 1.5% of El-Qaá total area represents zones very highly susceptible to landslides. The highly landslide-susceptible zones occupy 16.6% of El-Qaá area. All the highly landslide-susceptible zones are located in structurally controlled channels, rugged topography, and Precambrian basement rocks. The very high- and high-susceptible zones are distributed along several wadis in the study area such as Wadi Feiran, Wadi El-Aawag, Wadi Maier, Wadi Timan, Wadi Asla, and Wadi El-Mahasha. The moderate-, low-, and very low-susceptibility zones occupy 26.9, 35.7, and 19.3% of the total El-Qaá area, respectively. The geophysical studies support this study and reveal the depths and directions of major faults that may cause the landslides. The landslide occurrences are associated mainly with the NE-SW and NW-SE faults. The geophysical investigations indicate that the tectonic movements that caused the opening of Gulf of Aqaba and Gulf of Suez trigger the landslide events in El-Qaá area.

In short, most zones highly susceptibility to landslides are distributed in different locations around built-up communities. Hence, the development actions and management plans should consider these zones to reduce and compensate for greater hazards potential. The results of this study provide new locations susceptible to landslides. In short, this study recommends that decision makers apply mitigation efforts in El-Qaà area to avoid the socio-economic impacts of landslide hazards.

References

Abu El-Ata AS (1988) The relation between the local tectonics of Egypt and the plate tectonics of the surrounding regions using geophysical and geological data. Proceeding of the 6th Annual Meeting of Egyptian General Petroleum Corporation, Cairo, pp 92–112

Abuzied SM (2016) Groundwater potential zone assessment in Wadi Watir area, Egypt using radar data and GIS. Arab J Geosci 9(7):1–20. https://doi.org/10.1007/s12517-016-2519-2

Abuzied SM and Alrefaee HM (2017) Mapping of groundwater prospective zones integrating remote sensing, geographic information systems and geophysical techniques in El-Qaà Plain area, Egypt. Hydrogeol J 1–22. https://doi.org/10.1007/s10040-017-1603-3

Abuzied SM, Ibrahim SK, Kaiser MF, Saleem TA (2016a) Geospatial susceptibility mapping of earthquake-induced landslides in Nuweiba area, gulf of Aqaba, Egypt. J Mt Sci 13(7):1286–1303. https://doi.org/10.1007/s11629-015-3441-x

Abuzied SM, Ibrahim SK, Kaiser MF, Seleem TA (2016b) Application of remote sensing and spatial data integrations for mapping porphyry copper zones in Nuweiba area, Egypt. Int J Signal Process Syst 4(2): 102–108. https://doi.org/10.12720/ijsps.4.2.102-108

Abuzied SM, Yuan M, Ibrahim SK, Kaiser MF, Saleem TA (2016c) Geospatial risk assessment of flash floods in Nuweiba area, Egypt. J Arid Environ 133:54–72. https://doi.org/10.1016/j.jaridenv.2016.06.004

Abuzied SM, Yuan M, Ibrahim SK, Kaiser MF, Seleem TA (2016d) Delineation of groundwater potential zones in Nuweiba area (Egypt) using remote sensing and GIS techniques. Int J Signal Process Syst 4(2):109–117. https://doi.org/10.12720/ijsps.4.2.109-117

Ahmed M, Sauck W, Sultan M, Yan E, Soliman F, Rashed M (2014) Geophysical constraints on the Hydrogeologic and structural settings of the Gulf of Suez rift-related basins: case study from the El Qaa plain, Sinai, Egypt. Surv Geophys 35:415–430. https://doi.org/10.1007/s10712-013-9259-6

Aleotti P, Chowdhury R (1999) Landslide hazard assessment: summary review and new perspectives. Bull Eng Geol Environ 58(1):21–44. https://doi.org/10.1007/s100640050066

Azab AA, EL-Khadargy AA (2013) 2.5-D gravity/magnetic model studies in Sahl El Qaa area, southwestern Sinai, Egypt. Pure Appl Geophys 170:2207–222 9. https://doi.org/10.1007/s00024-013-0650-5

Baban SM, Sant KJ (2005) Mapping landslide susceptibility for the Caribbean island of Tobago using GIS, multi-criteria evaluation techniques with a varied weighted approach. Caribbean J Earth Sci 38:11–20

Bakhshipour Z, Huat BK, Ibrahim S, Asadi A, Kura NM (2013) Application of geophysical techniques for 3D Geohazard mapping to delineate cavities and potential sinkholes in the northern part of Kuala Lumpur, Malaysia. Sci World J 2013:1–11. https://doi.org/10.1155/2013/629476

Baranov V, Naudy H (1964) Numerical calculation of the formula of reduction to the magnetic pole. Geophys J 29(1):67–79. https://doi.org/10.1190/1.1439334

Benson AK, Floyd AR (2000) Application of gravity and magnetic methods to assess geological hazards and natural resource potential in the Mosida Hills, Utah County, Utah. Geophysics 65(5):1514–1526

Bogoslovsky VA, Ogilvy AA (1977) Geophysical methods for the investigation of landslides. Geophys J 42(3):562–571. https://doi.org/10.1190/1.1440727

Bonham-Carter GF, Agterberg FP (1999) Arc-WofE: a GIS tool for statistical integration of mineral exploration datasets. Bull Int Stat Inst 52:497–500

Brabb EE (1984) Innovative approaches to landslide hazard and risk mapping. Proceeding of the 4th International Symposium on Landslides, 16–21 September, Toronto, Ontario, Canada (Canadian Geotechnical Society, Toronto, Ontario, Canada), pp 307–324

Bughi S, Aleotti P, Bruschi R, Andrei G, Milani G, Scarpelli G (1996) Slow movements of slopes interfering with pipelines: modelling vs. monitoring. American Society of Mechanical Engineers, New York

Carrara A, Cardinali M, Detti R, Guzzetti F, Pasqui V, Reichenbach P (1991) GIS techniques and statistical models in evaluating landslide hazard. Earth Surf Proc Land 16(5):427–445. https://doi.org/10.1002/esp.3290160505

Chen Z, Wang J (2007) Landslide hazard mapping using logistic regression model in Mackenzie Valley, Canada. Nat Hazards 42(1):75–89. https://doi.org/10.1016/j.jappgeo.2005.09.001

Colletta BP, Le Q, Letouzey J, Moretti I (1988) Longitudinal variation of Suez rift structure (Egypt). Tectonophysics 153:221–233. https://doi.org/10.1016/0040-1951(88)90017-0

Conforti M, Aucelli PP, Robustelli G, Scarciglia F (2011) Geomorphology and GIS analysis for mapping gully erosion susceptibility in the Turbolo stream catchment (northern Calabria, Italy). Nat Hazards 56(3):881–898. https://doi.org/10.1007/s11069-010-9598-2

Conoco (1982) Getchell mine pit water volumes. Inter-office Communication from J.T, McDonough

Constantin M, Bednarik M, Jurchescu MC, Vlaicu M (2011) Landslide susceptibility assessment using the bivariate statistical analysis and the index of entropy in the Sibiciu Basin (Romania). Environ Earth Sci 63(2):397–406. https://doi.org/10.1007/s12665-010-0724-y

Cruden DM, Varnes DJ (1996) Landslide types and processes. In: Turner AK, Schuster RL (eds) Landslides investigation and mitigation. Transportation research board, US National Research Council. Special Report 247, Washington, DC, Chapter 3, pp 36–75

Dames and Moore (1985) Sinai Development Study, phase 1, Final Report, Water Supplies and Coast, Vol. Report submitted to the Advisory Committee for Reconstruction, Ministry of Development, Cairo 147p

Dayan U, Abramski R (1983) Heavy rain in the Middle East related to unusual jet stream properties. Bull Am Meteorolog Soc 64(10):1138–1140

De Vita P, Agrello D, Ambrosino F (2006) Landslide susceptibility assessment in ash-fall pyroclastic deposits surrounding mount Somma-Vesuvius: application of geophysical surveys for soil thickness mapping. J Appl Geophys 59(2):126–139. https://doi.org/10.1016/j.jappgeo.2005.09.001

Dennis SW (1984) The tectonic framework of petroleum occurrence in the Western Desert of Egypt. EGPC 7th exploration seminar Cairo

Dobrin MB (1976) Introduction to geophysical prospecting, 3rd edn. Mc Graw Hill Book Company, New York 630 p

Dobrin MB, Savit CH (1988) Introduction to geophysical prospecting, 4th edn. Mc Graw Hill Book Company, New York, 867p

El-Nahry AH, Saleh AM (2004) Influence of seasonal flashfloods on terrain and soils of El-Qaà plain, South Sinai, Egypt. Egypt J Soil Sci 44(4):489

Ercanoglu M, Gokceoglu C (2004) Use of fuzzy relations to produce landslide susceptibility map of a landslide prone area (west Black Sea region, Turkey). Eng Geol 75(3):229–250. https://doi.org/10.1016/j.enggeo.2004.06.001

Evans SG, Hungr O (1993) The assessment of rock fall hazards at the base of talus slopes. Can Geotech J 30:620–636

Farooq M, Park S, Song YS, Kim JH, Tariq M, Abraham AA (2012) Subsurface cavity detection in a karst environment using electrical resistivity (er): a case study from Yongweolri, South Korea. Earth Sci Res 16(1):75–82

Fasani GB, Bozzano F, Cardarelli E, Cercato M (2013) Underground cavity investigation within the city of Rome (Italy): a multi-disciplinary approach combining geological and geophysical data. Eng Geol 152:109–121. https://doi.org/10.1016/j.enggeo.2012.10.006

Feizizadeh B, Blaschke T (2013) GIS-multicriteria decision analysis for landslide susceptibility mapping: comparing three methods for the Urmia lake basin, Iran. Nat Hazards 65(3):2105–2128. https://doi.org/10.1007/s11069-012-0463-3

Forte F, Strobl RO, Pennetta L (2006) A methodology using GIS, aerial photos and remote sensing for loss estimation and flood vulnerability analysis in the Supersano-Ruffano-Nociglia graben, southern Italy. Environ Geol 50(4):581–594. https://doi.org/10.1007/s00254-006-0234-0

Galli M, Ardizzone F, Cardinali M, Guzzetti F, Reichenbach P (2008) Comparing landslide inventory maps. Geomorphology 94(3–4):268–289

Gemitzi A, Falalakis G, Eskioglou P, Petalas C (2011) Evaluating landslide susceptibility using environmental factors, fuzzy membership functions and GIS. Global NEST J 13(1):28–40

Geological Survey of Israel (1980) The aeromagnetic reduced to the North Pole map of Sinai Peninsula

Geosoft (2008) Oasis Montaj software package. Mapping and Processing system, Ontario, Canada

Gilboa Y (1980) Post Eocene clastics distribution along the El-Qaà plain, southern Sinai. J Earth Sci 29:197–206

Gorsevski PV, Gessler P, Foltz RB (2000) Spatial prediction of landslide hazard using discriminant analysis and GIS. Conference and Workshop: applications for the 21st Century, Denver, Colorado, September 25–27, 2000

Griffin WR (1949) Residual gravity in theory and practice. Geophysics 14(1):39–56

Guzzetti F, Malamud BD, Turcotte DL, Reichenbach P (2002) Power-law correlations of landslide areas in Central Italy. Earth Planet Sci Lett 195(3):169–183

Guzzetti F, Mondini AC, Cardinali M, Fiorucci F, Santangelo M, Chang KT (2012) Landslide inventory maps: new tools for an old problem. Earth Sci Rev 112(1–2):42–66

Hadji R, Errahmane Boumazbeur A, Limani Y, Baghem M, Chouabi AE, Demdoum A (2013) Geologic, topographic and climatic controls in landslide hazard assessment using GIS modeling: a case study of Souk Ahras region, NE Algeria. Quatern Int 302:224–237. https://doi.org/10.1016/j.quaint.2012.11.027

Hammad FA (1980) Geomorphological and hydrological aspects of Sinai Peninsula. Annal Geol Surv Egypt X:807–817

Hong Y, Adler R, Huffman G (2007) Use of satellite remote sensing data in the mapping of global landslide susceptibility. Nat Hazards 43(2):245–256. https://doi.org/10.1007/s11069-006-9104-z

Hunter JA, Burns RA, Good RL, Pullan SE, Pugin A, Crow H (2010) Near-surface geophysical techniques for geohazards investigations: some Canadian examples. Leading Edge 29(8):964–977. https://doi.org/10.1190/1.3480011

Ilanloo M (2012) Mass movements hazard zonation with analyzing hierarchy process (AHP) method (case study: Varenge Roud basin). Int J Agric Crop Sci 4(16):1159–1165

Kanungo DP, Sarkar S, Sharma S (2011) Combining neural network with fuzzy, certainty factor and likelihood ratio concepts for spatial prediction of landslides. Nat Hazards 59(3):1491–1512. https://doi.org/10.1007/s11069-011-9847-z

Kim JH, Yi MJ, Hwang SH, Song Y, Cho SJ, Synn JH (2007) Integrated geophysical surveys for the safety evaluation of a ground subsidence zone in a small city. J Geophys Eng 4(3):332–347. https://doi.org/10.1088/1742-2132/4/3/S12

Kornejady A, Kohzad H, Sarparast M, Khosravi G, Mombeini M (2014) Performance assessment of two "LNRF" and "AHP-area density" models in landslide susceptibility zonation. J Life Sci Biomed 4(3):169–176

Lahti I, Karinen T (2010) Tilt derivative multiscale edges of magnetic data. Leading Edge 29:24–29. https://doi.org/10.1190/1.3284049

Lee S, Min K (2001) Statistical analysis of landslide susceptibility at Yongin, Korea. Environ Geol 40(9):1095–1113. https://doi.org/10.1007/s002540100310

Lowrie W (2007) Fundamentals of geophysics, 2nd edn. Cambridge University Press, New York 381p

Malamud BD, Turcotte DL, Guzzetti F, Reichenbach P (2004) Landslide inventories and their statistical properties. Earth Surf Proc Landf 29(6):687–711

Malehmir A, Socco LV, Bstini M, Krawczyk CM, Pfaffhuber AA, Miller RD, Maurer H, Frauenfelder R, Suto K, Bazin S, Merz K, Dahlin T (2016) Near-surface geophysical characterization of areas prone to

natural hazards: a review of the current and perspective on the future. Adv Geophys 57:51–146

Mancini F, Ceppi C, Ritrovato G (2010) GIS and statistical analysis for landslide susceptibility mapping in the Daunia area, Italy. Nat Hazard Earth Syst Sci 10:1851–1864. https://doi.org/10.5194/nhess-10-1851-2010

Meshref WM (1990) Tectonic framework of Egypt. In: Said R (ed) The geology of Egypt. AA Balkema, Rotterdam, pp 113–156

Miller HG, Singh V (1994) Potential field tilt a new concept for location of potential field sources. J Appl Geophys 32:213–217. https://doi.org/10.1016/0926-9851(94)90022-1

Mohammadi M (2008) Mass movement hazard analysis and presentation of suitable regional model using GIS (Case Study: A part of Haraz Watershed). M.Sc. Thesis, Tarbiat Modarres University International Campus, Iran, pp 80

Moore ID, Burch GJ (1986) Sediment transport capacity of sheet and rill flow: application of unit stream power theory. Water Resour Res 22(8):1350–1360. https://doi.org/10.1029/WR022i008p01350

Moore ID, Grayson RB, Ladson AR (1991) Digital terrain modelling: a review of hydrological, geomorphological, and biological applications. Hydrol Process 5(1):3–30

Moore ID, Gessler PE, Nielsen GA, Peterson GA (1993) Soil attribute prediction using terrain analysis. Soil Sci Soc Am J 57(2):443–452

Mosconi A, Rebora A, Venturino G, Bocca P (1996) Egypt-Nile Delta and North Sinai Cenozoic tectonic evolutionary model - A proposal. Extended abstract, the 58th EAGE Conference and Exhibition. https://doi.org/10.3997/2214-4609.201409027

Moustafa AR, Abdeen MM (1992) Structural setting of the Hammam Faraun block, eastern side of the Suez rift. J Univ Kuwait Sci 19: 291–291

Nagarajan R, Mukherjee A, Roy A, Khire MV (1998) Technical note temporal remote sensing data and GIS application in landslide hazard zonation of part of western Ghat, India. Int J Remote Sens 19(4). https://doi.org/10.1080/014311698215865

Nilsen TH, Wright RH, Vlasic TC, Spangle W (1979) Relative Slope Stability and Landuse Planning in the San Francisco Bay Region, California, U.S. Geological Survey Professional Paper 944, US Government Printing Office, Washington, DC, pp 96

Noweir A, EL Shishtawy A (1996) Structure setting and stratigraphy of the area east of El-Qaà plain, southwestern Sinai, Egypt. J Geol 40(1):1–22

Oehler JF, Labazuy P, Lénat JF (2004) Recurrence of major flank landslides during the last 2-ma-history of Reunion Island. Bull Volcanol 66(7):585–598

Patton TL, Moustafa AR, Nelson RA, Abdine AS (1994) Tectonic evolution and structural setting of the Suez rift. In: Landon SM (ed) Interior rift basins, vol 59. AAPG, Memoir, pp 9–55

Pourghasemi HR, Pradhan B, Gokceoglu C, Moezzi KD (2012) Landslide susceptibility mapping using a spatial multi criteria evaluation model at Haraz watershed, Iran. In Terrigenous mass movements, Springer Berlin Heidelberg, Heidelberg, pp 23–49

Pradhan B, Lee S (2010) Delineation of landslide hazard areas on Penang Island, Malaysia, by using frequency ratio, logistic regression, and artificial neural network models. Environ Earth Sci 60(5):1037–1054. https://doi.org/10.1007/s12665-009-0245-8

Regmi AD, Devkota KC, Yoshida K, Pradhan B, Pourghasemi HR, Kumamoto T, Akgun A (2014) Application of frequency ratio, statistical index, and weights of evidence models and their comparison in landslide susceptibility mapping in Central Nepal Himalaya. Arab J Geosci 7(2):725–742. https://doi.org/10.1007/s12517-012-0807-z

Reid AB, Allsop JM, Granser H, Millett AJ, Somerton IW (1990) Magnetic interpretation in three dimensions using Euler deconvolution. Geophysics 55:80–91

Safaripour M, Monavari M, Zare M, Abedi Z, Gharagozlou A (2012) Flood risk assessment using GIS (case study: Golestan province, Iran). Pol J Environ Stud 21:1817–1824

Saha AK, Gupta RP, Arora MK (2002) GIS-based landslide hazard zonation in the Bhagirathi (ganga) valley, Himalayas. Int J Remote Sens 23(2):357–369. https://doi.org/10.1080/01431160010014260

Saha AK, Gupta RP, Sarkar I, Arora MK, Csaplovics E (2005) An approach for GIS-based statistical landslide susceptibility zonation-with a case study in the Himalayas. Landslides 2(1):61–69. https://doi.org/10.1007/s10346-004-0039-8

Said R (1962) The geology of Egypt. Elsevier Publication Co-operation, Amsterdam, 377p

Sankarapillai S, Aslam A (2013) Potential of GIS evaluation for mass wasting processes in mountain ranges of south west coast of India. J Earth Sci Eng 3(6):416

Santangelo Á, Cardinali Á, Rossi Á, Mondini AC, Guzzetti F (2010) Remote landslide mapping using a laser rangefinder binocular and GPS. Nat Hazards Earth Syst Sci 10(12):2539

Saraf AK, Choudhury PR (1998) Integrated remote sensing and GIS for groundwater exploration and identification of artificial recharge sites. Int J Remote Sens 19(10):1825–1841. https://doi.org/10.1080/014311698215018

Sarkar S, Kanungo DP (2004) An integrated approach for landslide susceptibility mapping using remote sensing and GIS. Photogramm Eng Remote Sens 70(5):617–625. https://doi.org/10.14358/PERS.70.5.617

Sharma PV (1997) Environmental and engineering geophysics. Cambridge University Press, Cambridge 475p

Sherief Y (2008) Flash floods and their effects on the development in El Qaa Plain area in south Sinai, Egypt-A Study in applied geomorphology using GIS and Remote sensing. Ph.D. Dissertation, Johannes Gutenberg Universität Mainz, 255p

Srivastava PK, Bhattacharya AK (2006) Groundwater assessment through an integrated approach using remote sensing, GIS and resistivity techniques: a case study from a hard rock terrain. Int J Remote Sens 27(20):4599–4620. https://doi.org/10.1080/01431160600554983

Sultan N and Halim MA (1988) Tectonic framework of northern Western Desert, Egypt and its effect on hydrocarbon accumulations. Proceeding of the 9th Exploration Conference (Egyptian General Petroleum Corporation Bulletin) Cairo, 2, pp 1–22

Sultan SA, Rahman NA, Ramadan TM, Salem SM (2013) The use of geophysical and remote sensing data analysis in the groundwater assessment of El Qaa plain, South Sinai, Egypt. Aust J Basic Appl Sci 7(1):394–400

Sun WF (2009) Study of landslide hazard assessment on typical loess area in Qianhe valley, Qianyang County. Ph.D. dissertation: Chinese Academy of Geological Science, Beijing

Suzen ML, Toprak V (1998) Filtering of satellite images in geological lineament analyses: an application to a fault zone in Central Turkey. Int J Remote Sens 19(6):1101–1114. https://doi.org/10.1080/014311698215621

Taramelli A, Melelli L, Pasqui M, Sorichetta A (2010) Modelling risk hurricane elements in potentially affected areas by a GIS system. Geomatics Natural Hazards Risk 1(4):349–373. https://doi.org/10.1080/19475705.2010.532972

Thompson DT (1982) EULDPH: a new technique for making computer-assisted depth estimates from magnetic data. Geophysics 47:31–37

Van Westen CJ, Rengers N, Terlien MTJ, Soeters R (1997) Prediction of the occurrence of slope instability phenomenal through GIS-based hazard zonation. Geol Rundsch Z Allg Geol 86(2):404–414. https://doi.org/10.1007/s005310050149

Varnes DJ (1978) Slope movement types and processes. In: Schuster RL, Krizek RJ (eds) Landslides, analysis and control, special report 176: transportation research board. National Academy of Sciences, Washington, DC, pp 11–33

Varnes DJ (1984) Landslide hazard zonation: a review of principles and practice, natural hazards 3, commission on landslides of the IAEG. UNESCO, Paris, p 63

Verduzco B, Fairhead JD, Green CM, MacKenzie C (2004) New insights into magnetic derivatives for structural mapping. Leading Edge 23: 116–119. https://doi.org/10.1190/1.1651454

Vlcko J, Wagner P, Rychlikova Z (1980) Evaluation of regional slope stability. Mineralia Slovaca 12(3):275–283

Wagner A, Leite E, Olivier R (1988) Rock and debris slides risk mapping in Nepal-A user friendly PC system for risk mapping. Proceeding of the 5th Intentional Symposium of Landslide, 10–15 July, Lausanne, Switzerland (AA Balkema, Rotterdam, the Netherlands), 2, pp 1251–1258

Wahid A, Madden M, Khalaf F, Fathy I (2009) Land suitability scenarios for arid coastal plains using GIS modeling: southwestern Sinai coastal plain, Egypt. J Urban Environ Eng 3(2):73–83. https://doi.org/10.4090/juee.2013.v3n2

Wang HB, Sassa K, Xu WY (2007) Assessment of landslide susceptibility using multivariate logistic regression: a case study in southern Japan. Environ Eng Geosci 13(2):183–192. https://doi.org/10.2113/gseegeosci.13.2.183

Yalcin A (2005) An investigation on Ardesen (Rize) region on the basis of landslide susceptibility, KTU. Ph.D. Thesis in Turkish

Yin KL and Yan TZ (1988) Statistical prediction model for slope instability of metamorphosed rocks. In: Bonnard C (Ed) Proceeding of the 5th International Symposium of Landslides, Lausanne, Balkema, Rotterdam 2, pp 1269–1272